Reduced order models of myelinated axonal compartments

Daniel Ioan[1] · Ruxandra Bărbulescu[1,2] · Luis Miguel Silveira[2] · Gabriela Ciuprina[1]

Abstract

The paper presents a hierarchical series of computational models for myelinated axonal compartments. Three classes of models are considered, either with distributed parameters (2.5D EQS–ElectroQuasi Static, 1D TL-Transmission Lines) or with lumped parameters (0D). They are systematically analyzed with both analytical and numerical approaches, the main goal being to identify the best procedure for order reduction of each case. An appropriate error estimator is proposed in order to assess the accuracy of the models. This is the foundation of a procedure able to find the simplest reduced model having an imposed precision. The most computationally efficient model from the three geometries proved to be the analytical 1D one, which is able to have accuracy less than 0.1%. By order reduction with vector fitting, a finite model is generated with a relative difference of 10^{-4} for order 5. The dynamical models thus extracted allow an efficient simulation of neurons and, consequently, of neuronal circuits. In such situations, the linear models of the myelinated compartments coupled with the dynamical, non-linear models of the Ranvier nodes, neuronal body (soma) and dendritic tree give global reduced models. In order to ease the simulation of large-scale neuronal systems, the sub-models at each level, including those of myelinated compartments should have the lowest possible order. The presented procedure is a first step in achieving simulations of neural systems with accuracy control.

1 Introduction

1.1 Myelinated axons

Myelination is an essential process in the formation of the nervous system. It begins before birth and continues until adolescence, resulting in increased neuronal performance, primarily in the transfer of neural signals along axons. Myelination consists of wrapping axons with an electri-

cally insulating layer, built by a series of glial cells (called Schwann cells). These cells have a lamellar shape and spiral wrap around the axons (Fig. 1), being composed of myelin, a protein-rich fat substance with good insulating properties. The space between two myelinated sections is called a Ranvier node. Having a high density of ion channels, these nodes are essential in regenerating the neuronal signal, previously attenuated during the transmission along myelinated compartments. The electrical phenomena occurring are linear in the myelinated sections and nonlinear in the Ranvier nodes. The neuronal signal transmitted along the myelinated axons seems to jump from node to node, a phenomenon called saltatory conduction. Among the first papers describing the saltatory conduction, Huxley and Stämpeli (1949) also presents how the characteristic parameters of the nerve fiber can be experimentally determined.

Although many consider the delay of internodal transmission negligible to the delay of signal reconditioning in the Ranvier nodes, it has been concluded that things are not exactly so (Villapecellín-Cid et al. 2004). The main objective of our study is the modeling in an accurate manner of the signal transmission between two Ranvier nodes
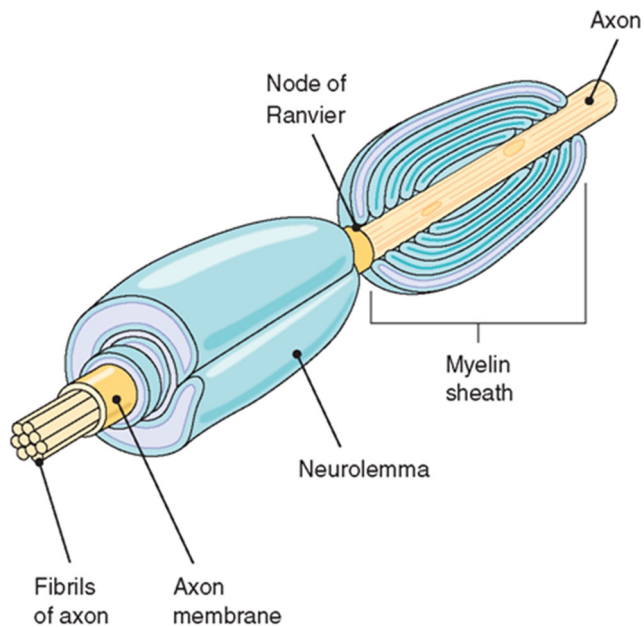

Action Editor: Arnd Roth

✉ Daniel Ioan
daniel@lmn.pub.ro

Luis Miguel Silveira
lms@inesc-id.pt

[1] University Politehnica of Bucharest, Splaiul Independentei 313, Bucharest 060042, Romania

[2] INESC-ID, Rua Alves Redol 9, 1000 Lisboa, Portugal

Fig. 1 The structure of myelinated axon (The Nervous System 2017)

through the myelinated section. The extraction of small size models with acceptable accuracy is essential for the simulation of saltatory conduction and consequently for the efficient simulation of impulse neural circuits, which are very complex circuits in the central and peripheral nervous system. In order to extract precise mathematical models of myelinated compartments, an exact knowledge of their morphology and material characteristics is necessary, as well as the complete understanding of the physico-chemical and bio-physiological phenomena that take place inside them.

1.2 Classification of neuronal models

The modeling of neurons and neuronal collections with high accuracy, by capturing the essential aspects of their functioning, and their efficient simulation have become central issues in neuroscience. These topics are presented in monographs of theoretical neuroscience (Izhikevich 2007; Keener and Sneyd 2010; Graham et al. 2011), in manuals of software simulators dedicated to neural systems (Bower and Beeman 1998; Carnevale and Hines 2006), or in articles describing various aspects such as: new neuronal models (Rattay et al. 2013), measurement of characteristic parameters (Van Geit et al. 2008), computational simulation methods (Moore et al. 1975).

The diversity of neural models reflects the complexity of the underlying problem of theoretical neuroscience. The models have various forms: mathematical models described with ordinary or partial derivative equations; electrical models described as systems or electrical circuits with lumped or distributed parameters. Any of them may be linear or nonlinear.

In the linear case, the equations can be represented in the frequency domain by applying suitable integral transformations (such as Fourier or Laplace) which allow the definition of transfer functions (called circuit functions in an electrical model, e.g. impedance, admittance, hybrid matrix), which greatly facilitate the study (Timotin 2004).

The complexity of a compact model is defined by its order, which is the number of state variables of the state equations. The models with lumped parameters, described by ODEs have a finite order, whereas models with distributed parameters, described by PDEs and transcendental transfer functions, have an infinite dimension of the state space. The model is represented as a dynamic input-output system, and it can be with a single input and a single output (SISO), such as transmission models for axons and dendrites, or multiple inputs and multiple outputs (MIMO), e.g. the ones used in the study of neurons with tree-like dendrites and axons. In order to describe the behavior of a multi-terminal model, the circuits theory can be used, to derive hybrid transfer matrices whose meanings depend on the way each terminal is controlled, either in current or in voltage. If the model is linear, the system representation can be the standard state space system of equations, with the matrices: A, B, C and D. This approach is suitable since the transmission of neural signals occurs unidirectionally. Since a typical neuron has an average of 10,000 synapses, it is obvious that the order reduction of its models should be made by preserving its tree-like structure. In particular, synapses, dendrites and axons are treated as SISO-type systems, whereas soma is MISO (multiple-inputs, single-output) and the axonal tree is SIMO (single-input, multiple-outputs). Otherwise, if the neuron would be treated as a MIMO system, it would result in tens of millions of input-output connections, whose descriptions would require important computing resources, even if they had a low order.

The simplest models are therefore those of neuronal signal transmission through axon or dendrite sections, RC models of minimal order, having lumped parameters describing longitudinal electrical conduction phenomena through axoplasm, and capacitive and transverse conductive effects through the cell membrane. In reality, these phenomena are distributed, so the precise model is the so-called "cable model", described by 1D PDEs of parabolic type (Lindsay et al. 1999). A common reduction method for these 1D models consists of segmenting the studied section into several compartments, each being minimally modeled with lumped parameters. Typically this modeling uses 5-10 compartments (Moore et al. 1978), so the global model called "behavioral" has the same number of capacitors included in the equivalent circuit.

Another category of models takes into account the electrochemical phenomena that occur in the ion channels

distributed in the cell membrane and which are active and nonlinear by excellence. The reference model in this category is Hodgkin-Huxley (HH) (Hodgkin and Huxley 1952), in which the dependence between the membrane current and the transmembrane voltage is described by four nonlinear ordinary differential equations, in which one describes a linear capacitive effect, having as state quantity the membrane voltage, and the other three describe the degree of ion channels opening. Since it does not contain any spatial variables to describe a spatial distribution, we say that this model is lumped, of 0D type. The simplified modeling of the membrane has received an intense scientific attention, so that there are several non-linear 0D models, of which the most commonly used are: FitzHugh – Nagumo (FN) (1966), Frankenhaeuser – Huxley (FH) (1964), Izhikevich (Iz) (2003). These models can be regarded as low-order approximations of the HH model, and are preferred in theoretical studies, precisely because of their relative simplicity.

For the modeling of axons, the 1D model of myelinated parts are linked to nonlinear 0D models of Ranvier nodes, resulting in non-linear PDEs (Keener and Sneyd 2010). This combination, in which the myelinated compartments are segmented and replaced with the simplest model, is the standard approach currently used to simulate saltatory conduction (Fitzhugh 1962; Rattay et al. 2013; Brown and Hamann 2014). This idea is implemented in most neural simulators (GENESIS, NEURON, etc.) (Bower and Beeman 1998; Carnevale and Hines 2006).

Other complicated models are reported in the literature, describing various morphological or structural details of neurons, such as the transition regions between Ranvier nodes and the axon body, called paranodes and juxtanodes (Brown and Hamann 2014; Ganapathy and Clark 1987) or the layered structure of myelin (Stephanova 2001), or the space between the neuron and this layer or between the layers (Young 2015).

Further development of these models is done by considering the spatial structure of neurons but also of the extracellular distribution of potential, which means the development of either 2D or 3D models. A first step is modeling the tree structures (Lindsay et al. 1999). For example, in Struijk et al. (1992), the spinal neurons and their collateral deviations are studied, considering the distribution of the extacellular potential estimated with finite differences. The extracellular potential distribution is also studied in Kuokkanen (2012), Joucla et al. (2014), and Parasuram et al. (2016). This distribution is important from several points of view: the interpretation of measurements made with electrodes placed in the extracellular space, the effect of partial demyelination and remyelination on the extracellular potential, the effect of stimulation by extracellular electrodes on the potential of action, as well as

for proper boundary conditions for our study. The problem of a non-myelinated active conducting fiber found in an infinite conducting homogeneous environment in which the scalar electric potential is harmonic is addressed in Clark and Plonsey (1966). The longitudinal component of the internal and external current was determined from the solution of the Laplace equation written in cylindrical coordinates using Bessel functions integrals. The extracellular potential and the current generated by a myelinated active fiber placed in a conductive medium is computed in Ganapathy and Clark (1987). The distribution of transmembrane voltage is determined as a solution of the Laplace equation in cylindrical coordinates. The distribution of the potential expressed as an integral of Bessel functions results after imposing the boundary conditions.

By combining the tree-like axon and dendrite models with the model of neuronal cell body (soma), the multi-terminal model of a single neuron is obtained. The next major step in neural system modeling is the study of neuronal collectivities. This step involves the modeling of synapses (Morrison et al. 2008; Keener and Sneyd 2010; Graupner and Brunel 2010). But as the number of simulated neurons grows, the problem becomes more and more difficult to solve, so it requires the use of a superior level of abstraction of single neuron behavior. This is why new theories were developed, such as artificial neural circuits (ANN), (Gurney 1997; Haykin 1999) and spiking neural networks (SNN), Maass (1997) and Paugam-Moisy and Bohte (2012). The goal is to model neural systems with the complexity of those found in the human brain. Simulations of networks with 16.7 million neurons with 4 billion synapses were performed (Digicortex 2017). If we only refer to the myelinated compartments, their number, virtually equal to that of the Ranvier nodes, is according to Brain Facts and Figures (2017) of 10^{11} only in brain.

Without a multiscale approach, where shifting from one level to another is done through a severe reduction of the order, it is not possible to address the problem of brain modeling (Robinson et al. 2005). This is the context, but also the explanation for the importance given to order reduction of myelinated compartments studied in this paper.

The following sections describe in a systematic way our study referring to the 2.5D models (Section 2), 1D models (Section 3) and 0D models (Section 4) of the myelinated compartments without Ranvier nodes. Each section presents one analytical and various numerical and model reduction approaches. In Section 6 the obtained results are discussed and compared so that an answer to the following questions can be given: 1) For an imposed order and model type (2.5D, 1D, 0D), which reduction method is the most accurate? 2) For an imposed error and model type, what method is able to reduce the model to the smallest order and what is this order? The answer to the second question is essential for the
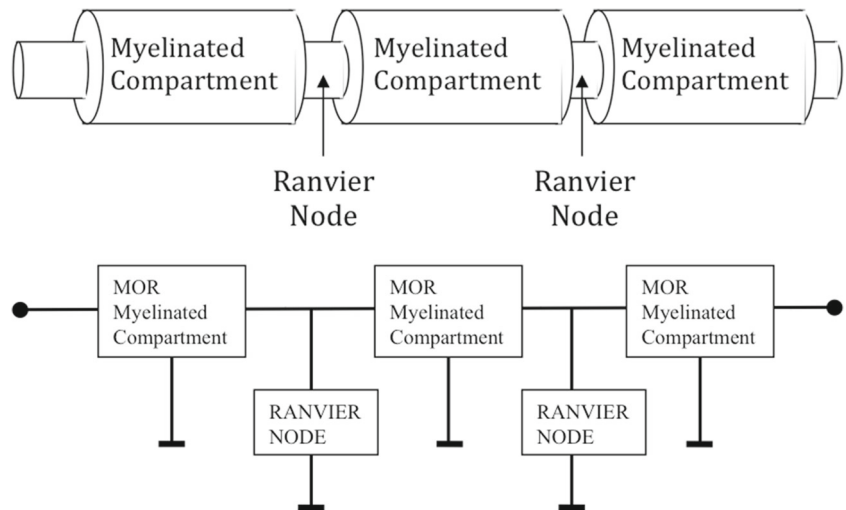
continuation of this research, in which our goal will be to connect the linear models of the myelinated compartments with the nonlinear models of the Ranvier nodes.

2 Axisymmetric (2.5D) models

2.1 Conceptual 2.5D model

The conceptual modeling of the axon starts from the simplified geometrical model shown in Fig. 2, from which the model of a cylindrical myelinated compartment is extracted (Fig. 3). The model is described by the following geometrical parameters: the cytoplasm radius – a, the outer radius of the compartment – b, the length of the myelinated compartment – L. A reference test case, with the following values is considered: $a = 7\,\mu$m; $b = 10\,\mu$m; $L = 0.25\lambda_0$ or λ_0 or $4\lambda_0$, $\lambda_0 = 223\,\mu$m; $\sigma_1 = 1.0824\,$S/m; $\sigma_2 = 2.04\cdot10^{-4}\,$S/m; $\varepsilon = 15.44\cdot\varepsilon_0$. The model is analyzed in the frequency range $f_m \leq f \leq f_M$, with the limits $f_m = 10^3$ Hz, and $f_M = 10^7$ Hz.

By carrying out a dimensional analysis of the material constants σ, ε, μ, the following characteristic times of the electromagnetic phenomena can be defined (Rapetti and Rousseaux 2014):

– $\tau_e = \varepsilon/\sigma$, the relaxation time of the charge and thus of the electric field in a conductor;

– $\tau_m = \mu\sigma L^2$, the diffusion time of the current and thus of the magnetic field in a conductor;

– $\tau_{em} = L/c$, having $c^2 = 1/(\varepsilon\mu)$, $\tau_{em}^2 = \tau_e\tau_m$, the time in which an electromagnetic wave with velocity c travels along the length L.

If we use the characteristic time τ (defined as duration, period, or time constant) to describe the speed of the analyzed phenomena, then it is possible to distinguish between rapid and slow EM field regimes. By considering the minimal and maximal values of the five characteristic parameters (σ, ε, μ, L, τ), we generated the map of EM field regimes function of characteristic times. The map indicates that the cytoplasm is operating in the ElectroConduction (EC) region, whereas the membrane has to be modeled with ElectroQuasiStatic (EQS) field.

2.2 Mathematical 2.5D model

In both domains of the compartment model the electric field is irrotational and thus an electric scalar potential can be defined. Due to the axial symmetry of the domain, this potential depends only on two spatial coordinates, the radius r and the axial position x. We will denote by V_1 the potential that corresponds to the cytoplasm and by V_2 the potential that corresponds to the membrane:

$$V(r,x) = \begin{cases} V_1, & \text{for } 0 < r < a. \\ V_2, & \text{for } a < r < b. \end{cases}$$

Fig. 3 Simplified geometrical model of the myelinated compartment
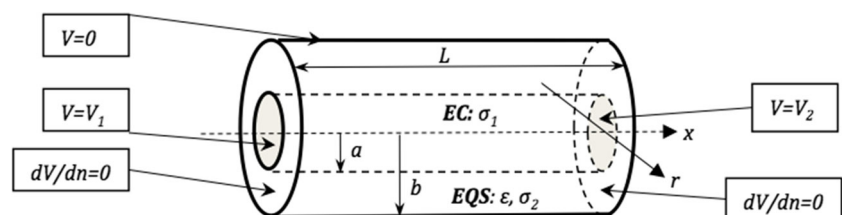
The field equations in the two sub-domains are:

$$\text{EC}: \begin{cases} \text{div}\mathbf{J} = 0 \\ \text{curl}\mathbf{E} = 0 \Rightarrow \mathbf{E} = -\text{grad}V_1 \Rightarrow \Delta V_1 = 0 \\ \mathbf{J} = \sigma_1 \mathbf{E}. \end{cases} \quad (1)$$

$$\text{EQS}: \begin{cases} \text{div}\mathbf{J} = -\partial \rho / \partial t \\ \text{div}\mathbf{D} = \rho \\ \text{curl}\mathbf{E} = 0 \Rightarrow \mathbf{E} = -\text{grad}V_2 \Rightarrow \Delta V_2 = 0 \\ \mathbf{J} = \sigma_2 \mathbf{E}, \mathbf{D} = \varepsilon \mathbf{E}, \end{cases}$$

where ρ is a generalized function of space. Therefore, $\Delta V_2(s) = 0$ in each subdomain, but not on the entire computing domain since on the discontinuity surface $r = a$ the following interface conditions are met:

$$V_1(a, x, t) = V_2(a, x, t) \Rightarrow V_1(a, x, s) = V_2(a, x, s);$$
$$\sigma_1 \frac{\partial V_1}{\partial n} = (\sigma_2 + \varepsilon s) \frac{\partial V_2}{\partial n}. \quad (2)$$

The solution $V(x, r, t)$ for $0 < x < L, 0 < r < b, 0 < t < t_{max}$ satisfies mixed boundary conditions:

$$\begin{cases} V(0, r, t) = V_1, & 0 < r < a; \\ V(L, r, t) = V_2, & 0 < r < a; \\ V(x, b, t) = 0, & 0 < x < L; \\ dV(0, r, t)/dn = 0, & a < r < b; \\ dV(L, r, t)/dn = 0, & a < r < b \\ \text{and } V(x, r, 0) = 0. \end{cases} \quad (3)$$

In reality, due to the ion pumps, in resting state (which in the formulation above would affect the initial condition) the potential has non-null value $V_0 = -70$ mV. We carried out the study for variations of the potential from this state of equilibrium, so the obtained dynamical system to be modeled and reduced is linear and not affine. These boundary conditions define a linear multipolar Electric Circuit Element (ECE, Ioan and Munteanu 1999) with distributed parameters, with three terminals, one being the ground and the other two voltage-controlled. Its dynamic behavior is fully described by the symmetrical matrix of operational admittances $\mathbf{Y}$, which has only two independent elements: the input admittance $Y_{11}(s) = Y_{22}(s)$ and the transfer admittance $Y_{12}(s) = Y_{21}(s)$, both complex functions of complex frequency s:

$$\mathbf{I}(s) = \mathbf{Y}(s)\mathbf{V}(s),$$
$$\text{with } \mathbf{I}(s) = \begin{bmatrix} I_1 \\ I_2 \end{bmatrix}; \mathbf{V}(s) = \begin{bmatrix} V_1 \\ V_2 \end{bmatrix}; \mathbf{Y}(s) = \begin{bmatrix} Y_{11} & Y_{12} \\ Y_{21} & Y_{22} \end{bmatrix}.$$

Here the input signals are the Laplace transforms of the terminals' potentials: $V_1(s) = \mathcal{L}[V(0, 0, t)]$, $V_2(s) = \mathcal{L}[V(L, 0, t)]$ and the output signals are the terminal's currents: $I_1(s) = \mathcal{L}[I_1(t)], I_2(s) = \mathcal{L}[I_2(t)]$.

2.3 Analytical 2.5D model

If the boundary conditions are slightly modified, so that on $x = 0$ and $x = L$ Neumann boundary conditions are set:

$$\begin{cases} \frac{dV}{dx}\Big|_{x=0} = \frac{I_1(t)}{\pi a^2 \sigma_1}, & 0 < r < a; \\ \frac{dV}{dx}\Big|_{x=L} = \frac{I_2(t)}{\pi a^2 \sigma_1}, & 0 < r < a; \\ V(x, b, t) = 0, & 0 < x < L; \\ \frac{dV}{dx}\Big|_{x=0} = 0, & a < r < b; \\ \frac{dV}{dx}\Big|_{x=L} = 0, & a < r < b; \\ V(x, r, 0) = 0, \end{cases}$$

the solution can be analytically determined, using the separation of variables. This change introduces a modeling error, due to the assumption that the current is uniformly distributed on each terminal, and therefore the terminal is no longer strictly equipotential. In reality, it is very likely that neither the potential nor the current density be perfectly constant on the terminal. The simplifying hypothesis of ignoring the radial variation of the current, which allows the derivation of an analytical solution, is acceptable, as this variation is expected to be small. The obtained radial variation of the potential can be used to compute an error estimator for the analytical method applied to this model called "non-ECE" in what follows. Since is excited in current, it will be characterized by an impedance matrix $\mathbf{Z} = \mathbf{Y}^{-1}$. The input impedance Z_{11} of the near terminal is computed as the ratio between the central potential $V(0, 0, s)$ and the injected current $I_1(s)$ under the assumption that the current of the far end terminal is null. The transfer impedance Z_{21} is the ratio of the potential at the center of the far end terminal $V(L, 0, s)$ and the current $I_1(s)$ injected into the near terminal, under the condition that the far end terminal current is null ($I_2 = 0$).

According to the proof in the Appendix it results that the potential has the following values in the electrodes centers:

$$V_1 = V(0, 0) = \sum_{k=1}^{m} \frac{F_k}{\lambda_k \text{th}(\lambda_k L)} R(0) = \frac{I_1}{\pi a} \sum_{k=1}^{m} \frac{J_1(\lambda_k a) \frac{B_k^2}{C_k^2}}{\|\lambda_k R_k\|^2 \text{th}(\lambda_k L)} \quad (4)$$

$$V_2 = V(0, L) = \sum_{k=1}^{m} \frac{F_k}{\lambda_k \text{sh}(\lambda_k L)} R(0) = \frac{I_1}{\pi a} \sum_{k=1}^{m} \frac{J_1(\lambda_k a) \frac{B_k^2}{C_k^2}}{\|\lambda_k R_k\|^2 \text{sh}(\lambda_k L)} \quad (5)$$

where $m = 200$ and F_k are the Fourier coefficients in the Fourier-Bessel series expansion of $\frac{\partial V}{\partial x}\Big|_{x=0}$, λ is the separation constant, $R(r)$ is decomposing $V(r, x)$ together with $X(x)$, J_1 represents the first order Bessel function of the first kind, B_k and C_k are integration constants.

They define the element's impedances $Z_{11} = V_1/I_1$ and $Z_{12} = V_2/I_1$. The radial variation of the potential on the near electrode is shown in Fig. 4. This variation is

Fig. 4 The radial variation of the potential at $x = 0$, computed analytically and numerically (FIT and FEM)
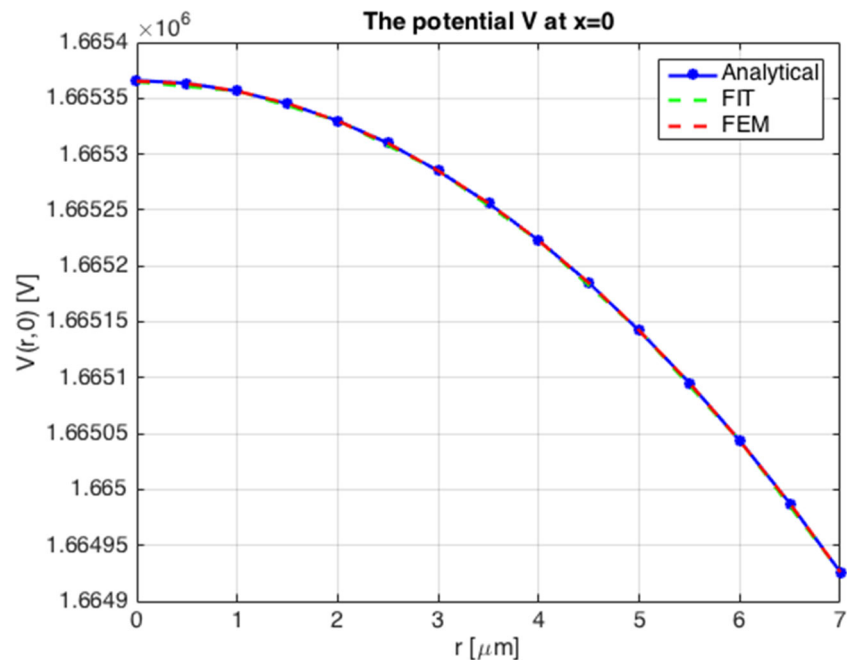
relatively negligible $\varepsilon_\infty = \varepsilon_m = (V(0,0) - V(a,0))/V_1 = (1.66537 - 1.66493)/1.66537 = 2.6 \cdot 10^{-4} = 0.026\%$.

The computational estimation of the analytical value is not affected only by this error but also by the method error of truncating the series and its approximation with a finite sum. Numerical tests show that the series (5) corresponding to the far end electrode has an exponential convergence, much faster than that corresponding to the near electrode (4). Table 1 shows the partial sums and the last term added to the sum of the analytical computation of potential $V(0,0)$. We note that even from the first term six significant digits are correct, and the fourth term adds another significant digit. The truncation error (computed as $\varepsilon_t = |V_m|/V_1$, where V_m is the mth term added to the truncated sum) is so small $\varepsilon_t = V_4/V_1 = 6.13 \cdot 10^{-6} \ll \varepsilon_m$, that the error of the analytical method $\varepsilon_a = \varepsilon_m + \varepsilon_t$ is given by the method error. Therefore, the summation of more than 2 terms in the series is useless, since the gain in accuracy is covered by the method error.

2.4 Numerical 2.5D model

The EC field problem was solved with an in-house Finite Integration Technique (FIT) code developed in MATLAB

Table 1 The convergence of the series for impedance Z_{11}, in bold the significant digits

m	Partial sum	Last term added
1	**1.665366**1913809199e+6	1.6653661913809199e+6
4	**1.6653657**945109792e+6	7.8181849318044057e+0
10	**1.6653659**660544212e+6	6.4287806450348339e-1

and with FEM (COMSOL) with three variants of boundary conditions: ECEv (ECE with voltage controlled equipotential terminals), ECEc (current controlled equipotential terminals), nonECEc (current controlled terminals, not equipotential, on which Neumann BCs are imposed).

In order to have a relevant comparison we have used for FIT and FEM the same discretization grid/mesh, regular and orthogonal, with quadrilateral FEM cells. Both FIT and FEM give in the case of the nonECEc boundary conditions very similar results with the analytical solution, as shown in Fig. 4, where the three curves overlap, which validates both numerical methods. The relative difference of $V(0,0)$ of FEM from the analytical solution is $5 \cdot 10^{-7}$. The values extracted from the ECE field problem have six significant digits common to those extracted from the nonECE field problem, which shows that the nonECE method error compared to ECE is even lower than $\varepsilon_m = 0.026\%$ estimated in the previous paragraph. The advantage of numerical methods is that they also allow the problem solving with ECE BCs. The difference between FIT and FEM solutions is as small as in the case of the nonECEc BCs. The two Dirichlet boundary conditions ECEv and ECEc give almost identical results, with 10 identical decimals for FEM, and 12 for FIT, respectively, which shows as expected that the excitation type (voltage or current) is not relevant in the ECE models.

The final results of the FIT and FEM numerical models were obtained by using component-wise Richardson extrapolation, of the results obtained for two discretization steps ($0.5 \, \mu$m and $1 \, \mu$m). The errors obtained lead us to consider the Richardson extrapolation for FEM as reference for computing the method errors (Table 2).

Table 2 Extrapolated values of conductances matrices (Y_{11} and Y_{12}) in d.c., for FIT and FEM, with 3 BCs

G_{FEM}-extrapolated	ECEv	ECEc	nonECEc
$G_{11} = Y_{11}(0)$	3.055380119410954e-6	3.055380119435735e-6	3.055379595174662e-6
$G_{12} = Y_{12}(0)$	−2.955775083424355e-6	−2.955775083450317e-6	−2.955775163682430e-6
G_{FIT}-extrapolated			
$G_{11} = Y_{11}(0)$	3.055380366776102e-6	3.055380366775098e-6	3.055620224050163e-6
$G_{12} = Y_{12}(0)$	−2.955775284972939e-6	−2.955775284973135e-6	−2.956014815660698e-6
Rel. diff. between extrap. values	$\|\mathbf{G}_{FIT} - \mathbf{G}_{FEM}\|/\|\mathbf{G}_{FEM}\|$	$\|\mathbf{G}_{FIT} - \mathbf{G}_{FEM}\|/\|\mathbf{G}_{FEM}\|$	$\|\mathbf{G}_{FIT} - \mathbf{G}_{FEM}\|/\|\mathbf{G}_{FEM}\|$
$\mathbf{G} = \mathbf{Y}(0)$	7.4680e-8	7.4686e-8	7.9980e-5

The relative error is approximated by an expression of type $c \cdot h^p$, where c and p are constants that describe the convergence rate and h is the discretization step. Considering two levels of mesh refinement, each halving the step h comparing to the precedent, the convergence rate p was derived. Table 3 holds the approximated constants c and p for FIT and FEM, with two different boundary conditions, ECE and nonECE. We can see that both FIT and FEM have a quadratic convergence order, FEM in the case of ECE having a relative error lower than FIT with about 2 orders of magnitude. In theory, quadratic FEM should have a higher convergence rate, but in practice it is limited because the boundary condition is not smooth at all being a non-continuous function (Jin 2015). Consequently, the reference values for the extracted circuit functions were given by the Richardson extrapolation of the FEM solution, for $p = 2$. The resulted values seem to have at least 8 exact significant figures. A better reference value may be obtained by using FEM with an adaptive mesh refinement.

Details on numerical solution with FEM The two subdomains with axial symmetry have rectangular shape in the coordinates (r, x) and start from radius eps: D1 = $(eps, a) \times (0, L)$; D2 = $(a, b) \times (0, L)$. They were meshed with a regular grid of squares with a step of 0.5 μm. For the axon radius of $b = 10 \mu$m, the radial mesh has (nxa+nxb-1) = 15+7-1 = 21 nodes and for longitudinal length $L = 0.25 \cdot \lambda_0 = 215 \mu$m/4 = 54 μm, the mesh has nx = 109 nodes, so a total of n = 2289 nodes. The mesh contains 2230 quadrilateral elements and $2 \times 2289 - 109 - 21 = 4448$ edges. In FEM, the base functions (also known as trial functions) for potential are second-order Lagrange polynomials,

**Table 3** The values of the constants c and p

$err_{rel} = c \cdot h^p$	ECE(v or c)	nonECE (c)
FIT	c = 4535e+3	c = 2.96e+14
	p = 1.95	p = 2.96
FEM	c = 39e+3	c = 14067e+3
	p = 2.00	p = 2.11

making each cell to have 9 degrees of freedom associated with the four vertices, edges' centers and cell center. The weak form of the equation solved is as follows: find $v \in H_D = \{v \in L^2(D) | \nabla v \in [L^2(D)]^3, v(S_D) = f_D\}$, where D = D1 ∪ D2. The affine Sobolev space, satisfying Dirichlet BC, so that:

$$a(v, u) = 2\pi \int_D \mathbf{J} \cdot \mathbf{E} r \, dA$$
$$= \int_0^b \int_0^L (\sigma + \varepsilon s)(\nabla v \cdot \nabla u) r \, dx \, dr$$

is null for any u having Dirichlet null BC. The number of DOFs is 9837, about four times larger than the number of nodes, as we expected. The use of second order elements makes the solution more precise than in the case of the first order, where the number of unknowns is the number of floating nodes (i.e. the inner ones plus those on the Neumann boundary, so that those with essential boundary conditions (Dirichlet) with known potential are excluded). The boundary conditions are as follows: null Dirichlet for $r = b$, $r < a$ and $x = L$, non-null Dirichlet of value $V_0 = 1$ for $r < a$ and $x = 0$ (essential), null Neumann in rest (natural). The system of linear algebraic equations
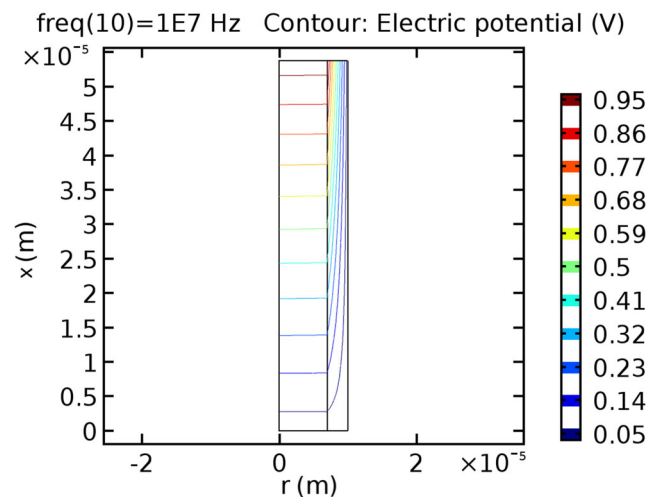
Fig. 5 Contour plots of the electric potential (FEM). The scales on the axis are not equal
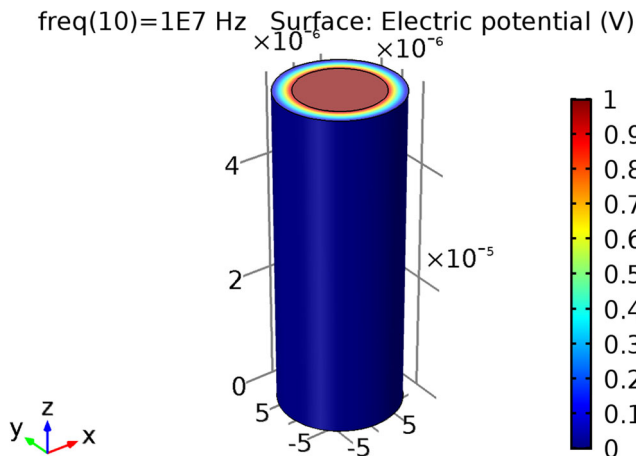
Fig. 6 The variation of the potential at the surface of the computing domain (FEM). The 3D image is obtained by rotating the 2D solution

obtained from $a(u, v) = 0$ by replacing u and v with their expansion in trial functions was solved with the direct solver MUMPS – MUltifrontal Massively Parallel Sparse direct Solver in 5 sec on a two-core MacOS system. The solution is graphically represented in Figs. 5 and 6.

The EQS analysis in the frequency range [1 kHz, 10 MHz] gives the frequency characteristics shown in Fig. 7.

Details on numerical solution with FIT The computing domain has been discretized with a mesh similar to that used in FEM. In stationary d.c. mode, each cell $(r_1, r_2) \times (z_1, z_2)$ contributes to the equations system with four conductances, placed on its four edges, having the expressions:

$$
\begin{cases}
G_{r1} = \frac{\pi\sigma((r_1+\Delta r_1)^2 - r_1^2)}{2\Delta z} \\
G_{r2} = \frac{\pi\sigma(r_2^2 - (r_2-\Delta r_2)^2)}{2\Delta z} & \text{for axial oriented} \\
G_{z1} = G_{z2} = \frac{\pi\sigma\Delta z}{\ln(r_2/r_1)} & \text{for radial oriented}
\end{cases} \quad (6)
$$

where the cell dimensions are: $\Delta z = z_2 - z_1$; $\Delta r = r_2 - r_1$; $\Delta r_1 = \Delta r_2 = \Delta r/2$; $G_{z1} = G_{z2} = 0$, if $r_1 = 0$.

The simplest implementation method in MATLAB uses the nodal technique to write the equations of this resistive electric circuit: $(\mathbf{AGA^T})\mathbf{V} = \mathbf{J}$, where $\mathbf{A}$ is the edges-nodes incidence matrix, $\mathbf{G}$ is the diagonal matrix of conductances (6) and $\mathbf{J}$ is the array of injected currents into nodes. The code is executed extremely fast since it does not contain *for* loops, but makes use of sparse matrices. The implementation is simplified if the nodes are numbered systematically from 1 to N, for example starting along the axis and then similarly for increasing radius, so that going through the nodes $i = 1 : nr-1$ and $j = 1 : nz-1$, all cells $k = (i-1)nz + j$ are covered. If the edges are numbered in agreement with the nodes, for example the axial ones having double indices $(2k)$ than the initial node (k) and the radial ones an uneven index $(2k+1)$, a total of $2N$ edges is obtained. Thus virtual edges are introduced on one

side of the boundary, which are removed eventually. They correspond to null columns in matrix $\mathbf{A}$. By splitting the node set into those floating, with unknown potentials ($\mathbf{V_1}$) and those placed on the Dirichlet boundary, with known potentials ($\mathbf{V_2}$) and considering the corresponding split of nodal conductances matrix:

$$
\begin{cases}
\mathbf{G_{11}V_1} + \mathbf{G_{11}V_2} = \mathbf{J_1} \\
\mathbf{G_{21}V_1} + \mathbf{G_{22}V_2} = 0
\end{cases} \Rightarrow \mathbf{G_{11}V_1} = \mathbf{J_1} - \mathbf{G_{11}V_2} \quad (7)
$$

leads to the system of linear equations that is solved to determine the unknown potentials ($\mathbf{V_1}$). Actually, this technique is also used in FEM to handle essential boundary conditions.

Under nonECEc boundary conditions, the injected current on the terminal is known, so the vector $\mathbf{J}$ is no longer null. The current injected into a circular crown between two successive nodes can be assigned to the initial node (case v1 in Fig. 8), to the final node (case v2), or the current injected into the node is calculated using the dual network edges as in dFIT (Ioan et al. 2006) (option 3). The results are presented comparatively in Fig. 8. The two alternatives 1 and 2 are bounds for the correct distribution, but the best numerical solution is obtained using the final version based on a dual network.

The EQS analysis requires minimal changes of the MATLAB code, namely the cell conductances G are replaced with their admittances, which are obtained by simply replacing the membrane conductivity σ_2 with $\sigma_2 + j\omega\varepsilon$. The results now depend on the frequency, and their representation in Fig. 7 overlaps those obtained with FEM, which validates both numerical methods FEM and FIT, in the case of ECE boundary conditions. The FEM solution is more accurate, but the computational effort is higher, since the system has four times more equations. To overcome this drawback, the dFIT approach can be used (Ioan et al. 2006), in which the unknowns are not only the potentials in nodes but also those in the center of the cells. The number of unknowns doubles, but the advantage is that two independent systems, each with n equations, are separately solved in parallel or sequentially for the two sets of potentials. Moreover, the two solutions realize a bracketing of the exact solution, allowing the control of the numerical computing error, since their difference is an upper bound of that error.

The EQS analysis needed a solving time of around 1.42 sec on a two-core MacOS system and used 1.604 MB of memory. There were 10 frequency samples computed, each one was solved with the direct solver UMFPACK, under Matlab.

This model is based on the assumption that the myelinated compartment can be represented by an equivalent perfectly symmetrical cylinder with constant radius. However, the cross-sectional profile of the axon may present

Fig. 7 The variation of Y_{11} and Y_{12} with frequency (FIT and FEM)
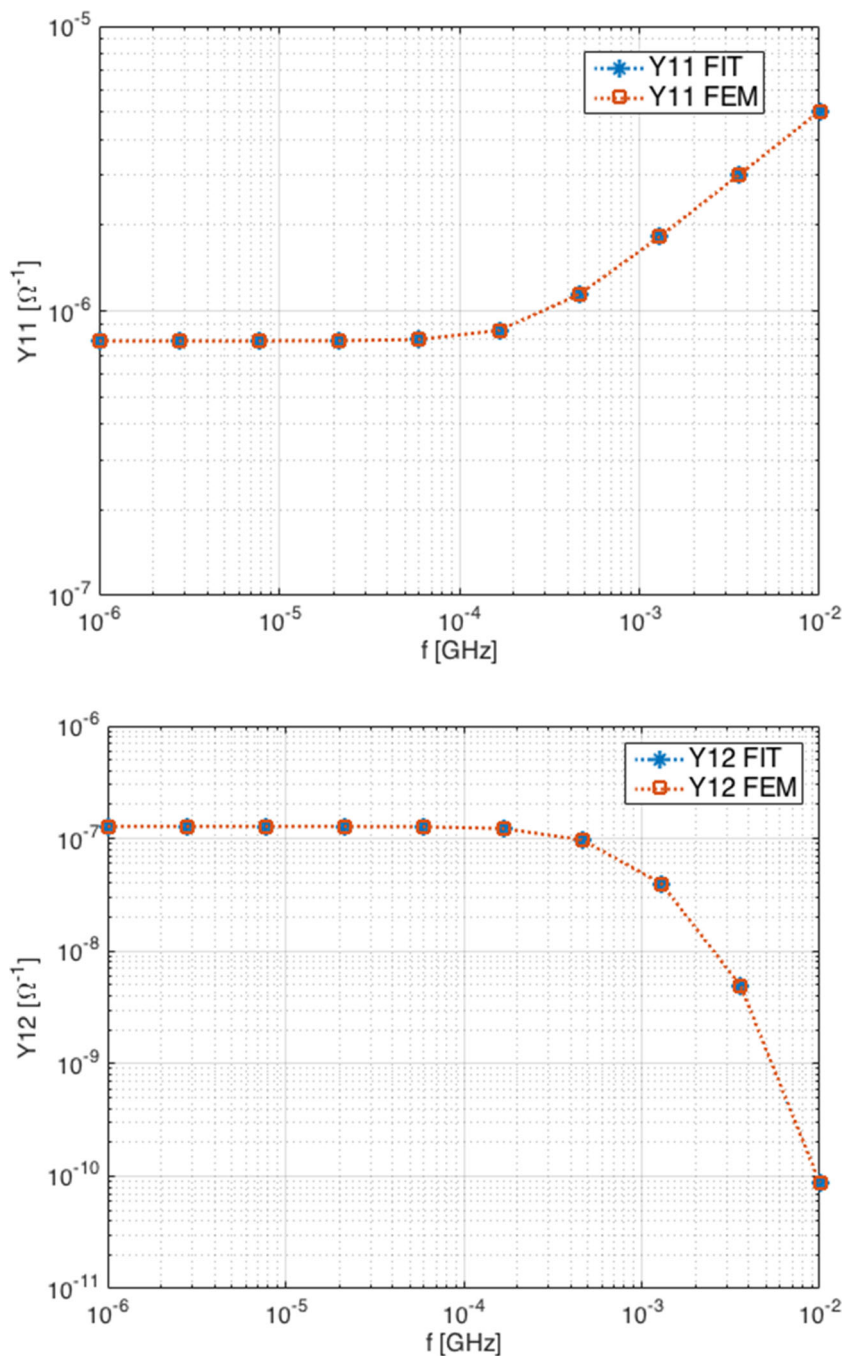

asymmetries (Halter and Clark 1991). A thorough analysis of asymmetries is not the object of this paper. It is expected that mild asymmetries of axons can be approximated with equivalent symmetrical axons. For this, an elliptic cylinder was considered, with the semimajor axis a_2 and semiminor axis a_1 preserving the initial cross-section area πa^2 (in the symmetrical model $a_1 = a_2 = a$) as in Fig. 9. The analysis of the relative error between the asymmetrical model $\mathbf{G}_{asym}$ and the symmetrical one $\mathbf{G}_{sym}$ with respect to the degree of eccentricity defined as a_2/a_1 (Fig. 10) shows a low influence of the asymmetry to the model's accuracy.

2.5 Order reduction of 2.5D models

In order to obtain simpler models valid for a large range of frequencies, methods such as VF Vector Fitting (VF) may be used (Gustavsen and Semlyen 1999). VF is a data-oriented reduction method, which searches for a rational approximation of the frequency characteristic given as a set of samples.

The order of the reduced system is imposed by the user and the result represents the best approximation of that order. Starting from a set of N_s circuit matrices $\mathbf{H} = \{\mathbf{H}_1,$
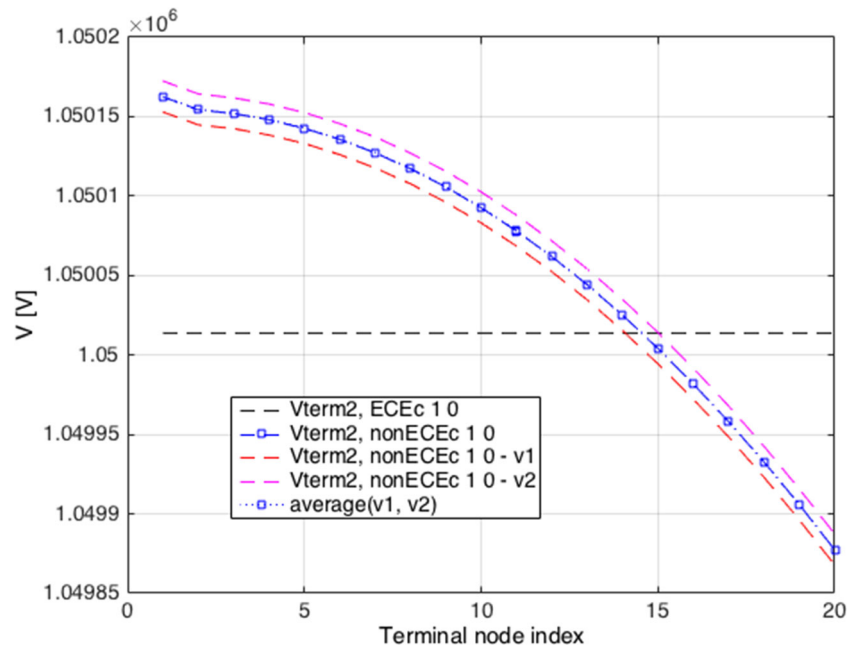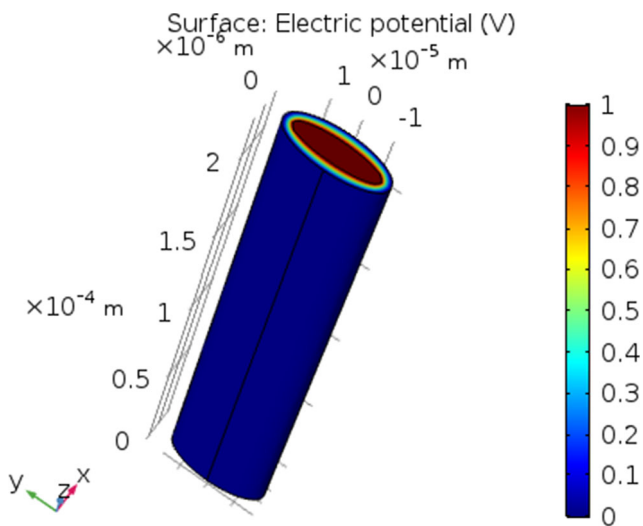
$\{\mathbf{H}_2, ..., \mathbf{H}_{N_s}\}$ of size $p \times p$ (in our case $p = 2$ and the matrices are positive defined and symmetrical), representing the admittances corresponding to the frequencies $s = [s_1, s_2, ..., s_{N_s}]$ with $s_k = j2\pi f_k$, it is aimed to iteratively determine the parameters of the rational matrix function in s:

$$\mathbf{Y}(s) = \mathbf{D} + s\mathbf{E} + \sum_{k=1}^{q} \frac{\mathbf{R}_k}{s - p_k}, \tag{8}$$

which approximates the data. It has q poles p_k, with residues $\mathbf{R}_k$ which are symmetrical complex matrices of dimension $p \times p$ and the real symmetrical matrices $\mathbf{D}$ and $\mathbf{E}$ of the same size. Using the data from the $N_s = 10$ frequency

samples represented in Fig. 7, reduced models of orders $q = 1, 2, 3, ..., 9$ were successively retrieved.

Figure 11 shows the relative errors of the reduced 2.5D model (with admittances Y_{11} and Y_{12}) with VF, for different line lengths and different orders q. Errors less than 10^{-10} are obtained for orders ranging from 4 to 8. For practical applications a order $q = 3 \div 5$ provides acceptable accuracy. For example, for $q = 3$ and $L = 2.5\lambda_0$, the three poles of the reduced model are $p_1 = -2.25 \cdot 10^8$, $p_2 = -2.30 \cdot 10^7$, $p_3 = -4.26 \cdot 10^6$ and the zeros are $z_1 = -2.61 \cdot 10^7$, $z_2 = -4.42 \cdot 10^6$. The real and negative values of the poles guarantee the stability and non-oscillating character of the reduced model. The conductance $G_{11} = 0.782 \cdot 10^{-6}$ of the reduced model has a deviation of 0.2% from the d.c. value of $Y_{11}(s)$.

3 Cable (1D) model

In this model the radial variation of the solution is neglected, so the potential $V(x, t)$ is dependent only of the axial position x and time t. This 1D spatial variation leads to the simplification of the potential equation, leading to the equations of the transmission lines (TLs), this model being also named the "cable model". This model is characterized by the per unit length (p.u.l.) parameters: r – longitudinal resistance, c – transversal line capacitance and g – transversal line conductance:

$$r = 1/(\sigma_1 \pi a^2); \tag{9}$$
$$c = \varepsilon 2\pi / \ln(b/a); \tag{10}$$
$$g = \sigma_2 2\pi / \ln(b/a), \tag{11}$$

Fig. 9 The asymmetrical FEM model, as an elliptic cylinder

Fig. 10 Relative error vs. degree of eccentricity of the asymmetrical model. EC case, $L = \lambda_0$, solved with FEM, error defined as $\|\mathbf{G}_{\text{asym}} - \mathbf{G}_{\text{sym}}\|/\|\mathbf{G}_{\text{sym}}\|$
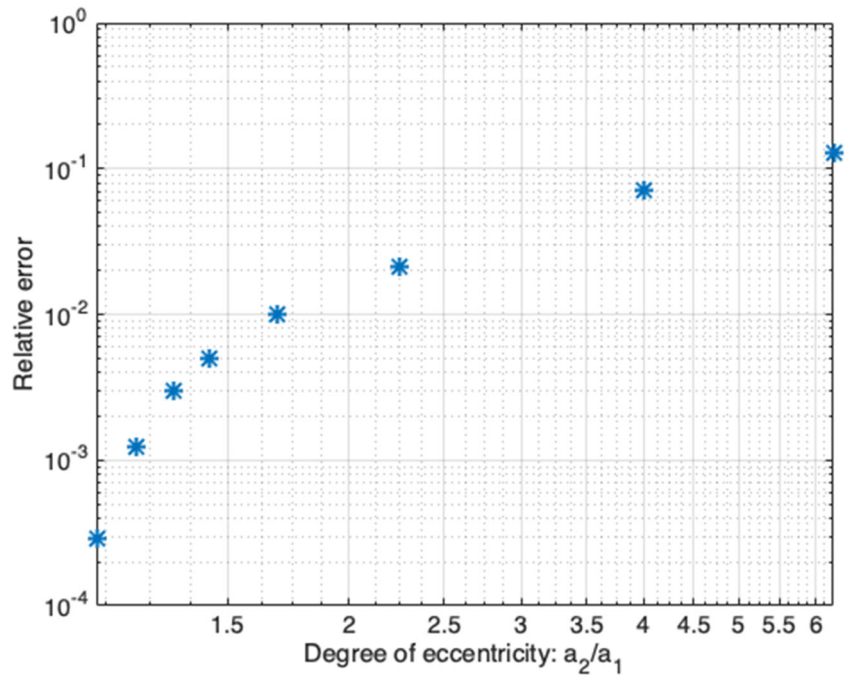
Fig. 11 The relative errors of the reduced model (Y_{11} and Y_{12}) with vector fitting
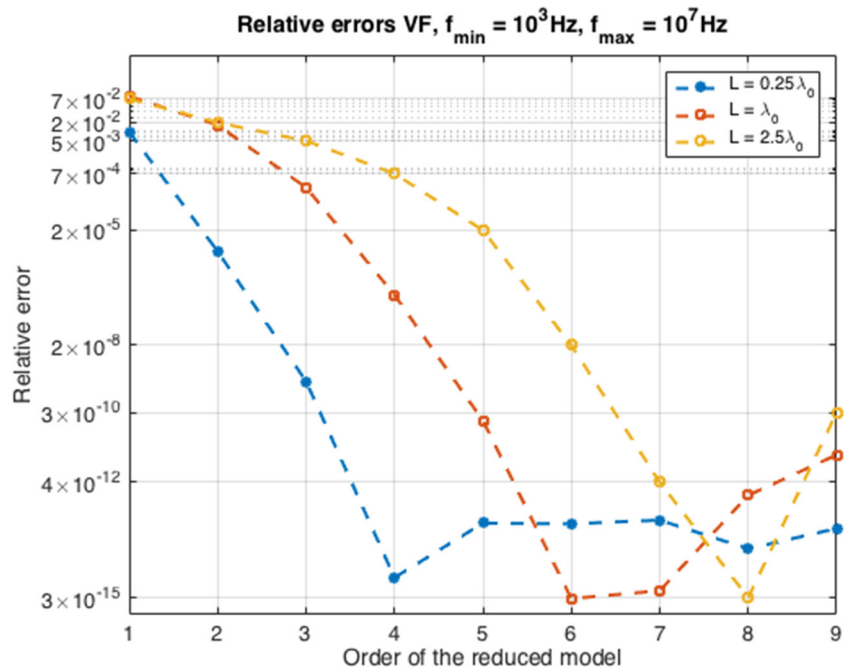
Fig. 12 Mapping the geometrical model with a segmented line circuit model

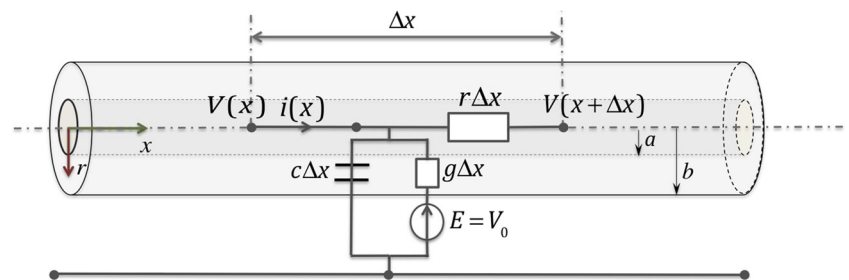which have in this test case the following values: $r = 6\,\mathrm{G}\Omega/\mathrm{m}$, $c = 2.4\,\mathrm{nF/m}$, $g = 3.59\,\mathrm{mS/m}$.

The geometrical 1D model mapped with a segmented line circuit model having length Δx is shown in Fig. 12. In this circuit the voltage source $E = V_0 = -70$ mV is considered to describe the effect of ion channels (Niebur 2008).

By applying the Kirchhoff's laws and considering $\Delta x \to 0$, the first order PDE system is obtained:

$$-\frac{\partial i(x,t)}{\partial x} = g(V(x,t) - V_0) + c\frac{\partial V(x,t)}{\partial t}; \quad (12)$$

$$-\frac{\partial V(x,t)}{\partial x} = r i(x,t), \quad (13)$$

which leads to the second order PDE for potential:

$$\frac{\partial^2 V(x,t)}{\partial x^2} = rg(V(x,t) - V_0) + rc\frac{\partial V(x,t)}{\partial t}, \quad (14)$$

with $V(x,0) = V_0$, $V(0,t) = V_1(t)$, $V(L,t) = V_2(t)$.

Introducing the characteristic time $\tau = c/g = 0.67\,\mu s$ and the characteristic length $\lambda_0 = 1/\sqrt{rg} = 215\,\mu m$, Eq. (14) becomes:

$$\tau\frac{\partial V(x,t)}{\partial t} - \lambda_0^2\frac{\partial^2 V(x,t)}{\partial x^2} = V_0 - V(x,t). \quad (15)$$

This diffusion equation of parabolic type (similar to the heat equation) can be obtained also as a consequence of the EC-EQS field equations: charge conservation, electromagnetic induction law and material equations in 1D geometric assumption. The second order ODE of potential in the frequency domain is obtained through Laplace transform:

$$-\lambda_0^2\frac{\partial^2 V(x,s)}{\partial x^2} + (1 + \tau s)V(x,s) = \frac{V_0}{s} + \tau V(x,0), \quad (16)$$

in which $s = j\omega$, with $\omega = 2\pi f$ for the harmonic regime, at frequency f.

The characteristic time gives information about the system's major time constant, and the characteristic length shows the length above which the attenuation begins to have significant values. Our studies (Bărbulescu et al. 2016) have shown that the maximum line length of a myelinated compartment for which the neuronal signal is able to trigger the action potential is:

$$L_{max} = \lambda_0\mathrm{argcosh}\left(\frac{V_{max} - V_0}{V_t - V_0}\right) \cong 2.58\lambda_0,$$

where $V_{max} = 30$ mV is the maximum value of the neuronal signal, $V_0 = -70$ mV is the equilibrium potential and $V_t = -55$ mV is the threshold potential.

According to the literature, the typical length of a myelinated compartment is between $1 \div 2.5$ mm. This corresponds to an optimal length of about 100 times larger

than the external diameter of an axon (Fitzhugh 1962; Goldman and Albus 1968):

$$L_{opt} = (1 \div 2.5) \cdot 10^{-3} < L_{max} \cong 2.58\lambda_0$$
$$\Rightarrow \lambda_0 > \frac{(1 \div 2.5)}{2.58}\,\mathrm{mm} = (0.4 \div 1)\,\mathrm{mm}. \quad (17)$$

This means that the characteristic length should be larger than 0.4 mm. In our test case it is equal to 0.215 mm, but this value can be easily doubled if the parameters r and g are doubled (by modifying the material parameters σ_1 and σ_2 within the acceptable ranges).

3.1 Analytical 1D model

Considering a line having the length L as a two-port, excited in terminal voltages, the global dynamic admittance matrix is extracted, after solving (14) with zero initial conditions (Ciuprina et al. 2015):

$$\mathbf{Y}(s) = \begin{bmatrix} Y_{11} & Y_{12} \\ Y_{21} & Y_{22} \end{bmatrix} = \begin{bmatrix} \frac{\mathrm{ch}(\gamma L)}{Z_C\mathrm{sh}(\gamma L)} & -\frac{1}{Z_C\mathrm{sh}(\gamma L)} \\ -\frac{1}{Z_C\mathrm{sh}(\gamma L)} & \frac{\mathrm{ch}(\gamma L)}{Z_C\mathrm{sh}(\gamma L)} \end{bmatrix}; \quad (18)$$

$$\begin{bmatrix} I(0,s) \\ I(L,s) \end{bmatrix} = \begin{bmatrix} Y_{11} & Y_{12} \\ Y_{21} & Y_{22} \end{bmatrix}\begin{bmatrix} V(0,s) - V_0/s \\ V(L,s) - V_0/s \end{bmatrix}. \quad (19)$$

The characteristic line parameters $\gamma = \sqrt{r(g + sc)} = \sqrt{1 + \tau s}/\lambda_0$ and $Z_C = \sqrt{r/(g + sc)} = 1/(g\lambda_0\sqrt{1 + \tau s})$ do not depend on the line length. In the static regime ($s = 0$), $\gamma = \sqrt{rg} = 4.64 \cdot 10^3\,\mathrm{m}^{-1}$ and $Z_C = Z_0 = \sqrt{r/g} = 1/(g\lambda_0) = 1.29\,\mathrm{M}\Omega$.

The linear model described by these complex admittances has an equivalent circuit with an infinite number of capacitances and resistances. Voltage sources having e.m.f. $E = V_0$ have to be connected in series with the input ports to satisfy (16). Table 4 contains the asymptotic values of admittances vs. frequency.

The frequency characteristics of the 1D model $Y_{11}(f) = |\mathrm{Y}_{11}(j\omega)|$, $Y_{12}(f) = |\mathrm{Y}_{12}(j\omega)|$, $\omega = 2\pi f$, for two lengths: $L = \lambda_0/4$ and $L = 2.5\lambda_0$, are shown in Fig. 13. The dotted lines are the reference values, extracted from the numerical 2.5D FEM model. The two models give similar results over the entire frequency range.

The two circuit functions Y_{11} and especially Y_{12} determine the voltage attenuation factor of the transmitted

Table 4 The asymptotic limits for Y_{11} and Y_{12}

L	Y_{11}, Y_{12} for $f \to 0$	Y_{11}, Y_{12} for $f \to \infty$
$L \to 0$	$Y_{11} \to \infty, Y_{12} \to \infty$	∞, ∞
$L = \lambda_0$	$Y_{11} = \mathrm{th}(1)/Z_0, Y_{12} = 1/Z_0$	$\infty, 0$
$L \to \infty$	$Y_{11} = 1/Z_0, Y_{12} \to 0$	$Y_{11} \to \infty, Y_{12} \to 0$

Fig. 13 The frequency characteristics, $Y_{11}(f)$, $Y_{12}(f)$ for $L = \lambda_0/4$ (top) and $L = 2.5\lambda_0$ (bottom), computed with Eq. (18)
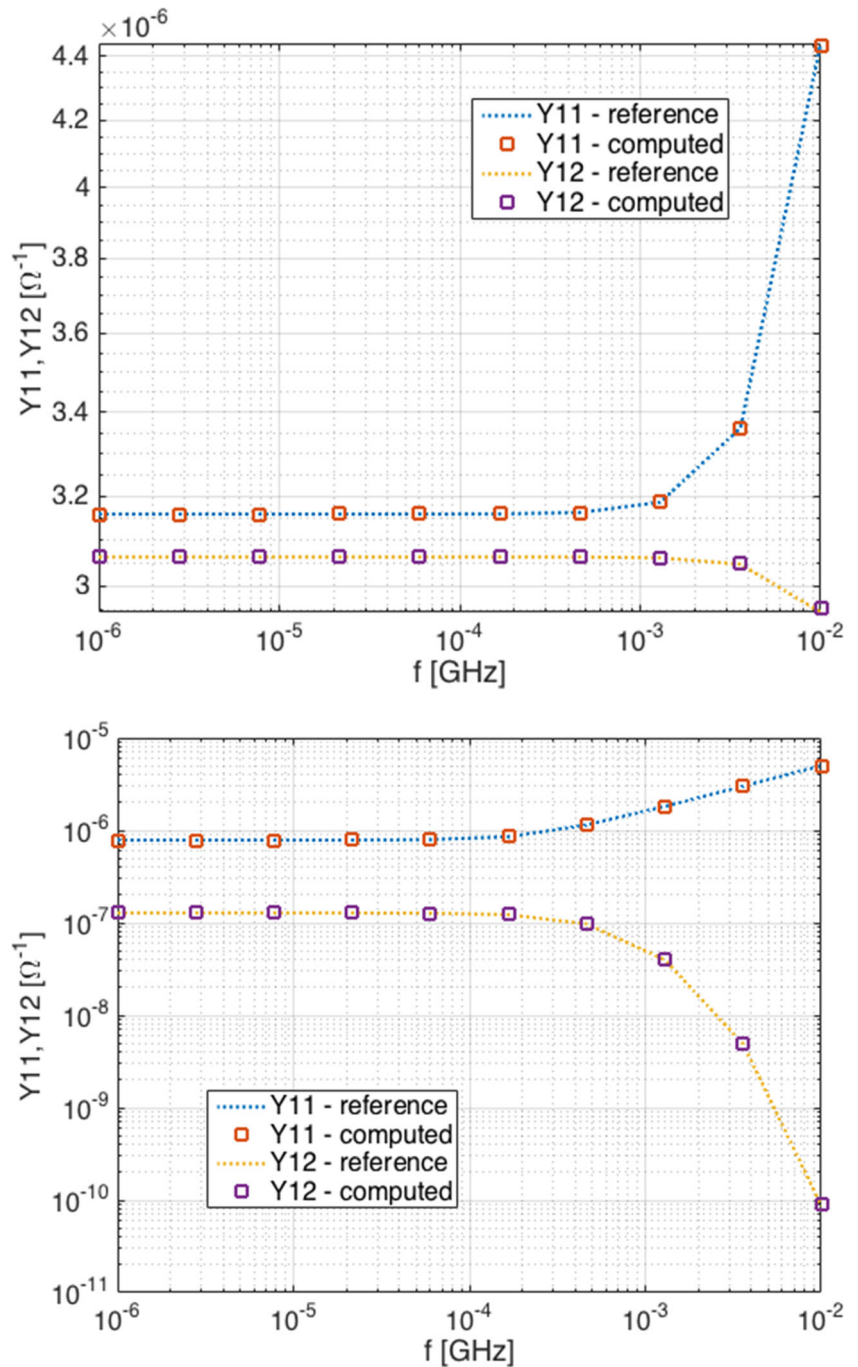
signal, which is the system's transfer function when the output terminal has a null current:

$$I(L, s) = Y_{21}(s)V(0, s) + Y_{22}(s)V(L, s) = 0 \Rightarrow$$

$$A_v(s) = \frac{V(L, s)}{V(0, s)} = -\frac{Y_{21}(s)}{Y_{22}(s)} = \frac{1}{\text{ch}(\sqrt{1 + s\tau}L/\lambda_0)}.$$

In stationary regime, the signal attenuation is $A_0 = A_v(0) = 1/\text{ch}(L/\lambda_0)$. The system acts as a low-pass filter, with $A_v(s) \xrightarrow{s \to \infty} 0$ and an infinity of poles s_k, all real and negative and satisfying the relation: $s_k\tau + 1 =$

$((k - 1/2)\pi\lambda_0/L)^2$, the first being essential. The small length compartment does not attenuate the input voltage in stationary regime, Y_{11} and Y_{12} being practically equal. As expected, the attenuation is higher for larger line lengths, six times higher for $L = 2.5\lambda_0$ than for short line.

Low frequency errors are very different from errors computed at high frequencies. Under these conditions, the global error estimate by the classical method gives completely irrelevant results. Therefore it is necessary to define the error differently. The typical neuronal signal has

Table 5 The relative errors of the analytical 1D model

Length L	$\varepsilon_{rel}[\%]$, Y_{11}	$\varepsilon_{rel}[\%]$, Y_{12}
$L = \lambda_0/4$	0.079	0.09
$L = \lambda_0$	0.055	0.027
$L = 2.5\lambda_0$	0.057	0.003

a spectrum in which the low frequency components are much more significant than the high frequency ones. In order to correctly quantify the error, a weighted norm $w(f)$, adequately defined is proposed (Stoica et al. 2005):

$$\|\mathbf{Y}\|_w \cong \int_{f_m}^{f_M} w(f)\|\mathbf{Y}(f)\|_2 \mathrm{d}f \cong \sum_{k=0}^{M} w(f_k)\|\mathbf{Y}(f_k)\|_2 \Delta f_k.$$

Here $\|\mathbf{Y}\|_2$ is the Euclidian norm of the matrix $\mathbf{Y}$ and the weight $w(f)$ is computed from the spectrum $w'(f)$ of the standard neuronal signal $s(t)$:

$$w'(f) = \left| \int_0^\infty s(t)e^{-j2\pi ft}\mathrm{d}t \right|$$

$$\cong \frac{t_{max}}{N} \left| \sum_{k=0}^{N} s\left(kt_{max}/N\right) e^{-j2\pi fkt_{max}/N} \right|;$$

$$W = \int_0^\infty w'(f)\mathrm{d}f \cong \int_{f_m}^{f_M} w'(f)\mathrm{d}f \cong \sum_{k=0}^{M} w'(f_k)\Delta f_k.$$

Thus the normalized weight $w(f_k) = w'(f_k)/W$ has a unitary integral. Considering the weighted norm, the global error is defined as:

$$\varepsilon_{rel} = Z_0 \|\mathbf{Y}_{1D} - \mathbf{Y}_{2.5D}\|_w, \tag{20}$$

where $Z_0 = 1/(g\lambda_0)$ is the d.c. characteristic impedance of the line.

Table 5 contains the relative errors between the 1D model and the reference 2.5D FEM model for Y_{11} and Y_{12}, computed with Eq. (20) for 10 frequencies between f_m and f_M, for different line lengths.

The general conclusion is that the 1D "cable model" correctly describes the transmission of the neuronal signal through the myelinated compartment, having numerical deviations from the field model of under 0.1%, even smaller for optimal lengths of real compartments (which is larger than the characteristic length). Consequently, if a better accuracy is required, the cable model is not acceptable and 2.5D field models should be used, but for the most practical cases this accuracy is acceptable.

3.2 Order reduction by series truncation of the analytical 1D model

The hyperbolic functions which compose the analytical model can be expanded in different infinite series and products (Abramowitz et al. 1988):

$$\frac{1}{\mathrm{sh}(z)} = \frac{1}{\sum_{k=0}^\infty \frac{z^{2k+1}}{(2k+1)!}} = \frac{1}{z} + 2z\sum_{k=1}^\infty \frac{(-1)^k}{z^2 + \alpha_k^2}$$

$$= \frac{1}{z\prod_{k=1}^\infty \left(1 + \left(\frac{z}{\alpha_k}\right)^2\right)}, \alpha_k = k\pi; \tag{21}$$

$$\mathrm{cth}(z) = \frac{\sum_{k=0}^\infty \frac{z^{2k}}{(2k)!}}{\sum_{k=0}^\infty \frac{z^{2k+1}}{(2k+1)!}} = \frac{1}{z} + 2z\sum_{k=1}^\infty \frac{1}{z^2 + \alpha_k^2}$$

$$= \frac{\prod_{k=1}^\infty \left(1 + \left(\frac{z}{\beta_k}\right)^2\right)}{z\prod_{k=1}^\infty \left(1 + \left(\frac{z}{\alpha_k}\right)^2\right)}, \beta_k = (2k-1)\pi/2. \tag{22}$$

The first way of expressing the hyperbolic functions in Eqs. 21 and 22 is a series of powers (Taylor-Padé for the numerator and denominator), the second is a series of simple fractions, and the last is a product of poles and zeros. Consequently, this model has an infinite divergent sequence of poles, distributed in an arithmetic progression on the negative semi-axis, the zeros being intercalated in-between the poles. We should notice that α_k are exactly the proper values of the spatial operator of the transmission equation, so they represent the modal characteristics of this equation.

Different reduced models – characterized by rational functions – are obtained by truncating these series to q terms. The first q poles of these functions have the smallest absolute value and they represent the most relevant poles of the original function. The truncation of the power series modifies the position of the poles, possibly generating complex poles, as it happens very early in the test case, for $q = 3$. The big advantage of these reducing approaches is that the reduced model is natively parametric. For example, reducing with simple fractions gives:

$$Y_{11}(s) = \frac{\mathrm{cth}(\gamma L)}{Z_C} \simeq \frac{g\lambda_0^2}{L}\left(1 + 2\sum_{k=1}^q \frac{s\tau + 1}{s\tau + 1 + (\alpha_k\lambda_0/L)^2}\right).$$

Unfortunately, the truncation in simple fractions of Y_{12} has a very slow convergence; therefore it is preferable to use Taylor-Padé or infinite product truncation for this circuit function. Besides the methods presented above, there is also the possibility to use continuous fractions expansion (authentic Padé) (Lozier 2003), which ensures moments' conservation and is expected to have the fastest

Fig. 14 Relative error of the 1D cable model reduced by series truncation vs. order of the reduced model, $L = 2.5\lambda_0$
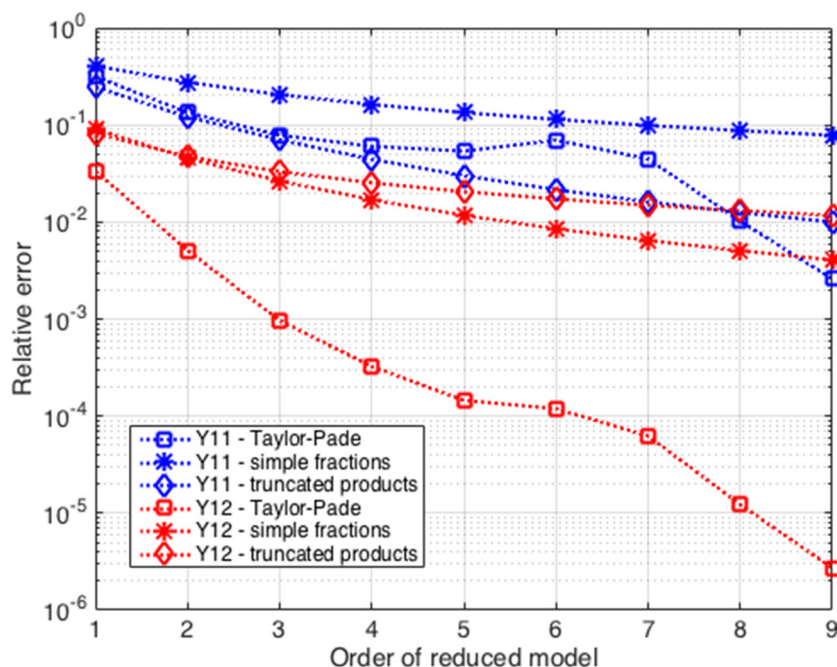

convergence. In our test case, this method gave best results (minimal errors) for order 10, but for order 3 the errors were between Taylor-Padé and simple fractions.

For the line lengths of interest, truncating the series of powers and truncating the infinite products proved to be the best reducing methods. The latter may be because truncating

Table 6 The relative errors of the reduced analytical 1D model vs. its order, Y_{11} and Y_{12}

Length L	$\varepsilon_{rel}[\%]$ $q = 1$	$\varepsilon_{rel}[\%]$ $q = 3$	$\varepsilon_{rel}[\%]$ $q = 10$
Y_{11}			
$\lambda_0/4$, simple fractions	4.81	2.11	0.71
λ_0, simple fractions	18.83	8.45	2.84
$2.5\lambda_0$, simple fractions	40.61	20.52	7.09
$\lambda_0/4$, Taylor-Padé	0.36	1.68e-4	1.2e-13
λ_0, Taylor-Padé	9.13	1.04	8.28e-9
$2.5\lambda_0$, Taylor-Padé	31.62	7.85	0.05
$\lambda_0/4$, truncated products	1.11	0.18	0.018
λ_0, truncated products	7.82	1.39	0.14
$2.5\lambda_0$, truncated products	24.57	7.00	0.81
Y_{12}			
$\lambda_0/4$, simple fractions	1.32	0.28	0.03
λ_0, simple fractions	5.04	1.14	0.13
$2.5\lambda_0$, simple fractions	9.11	2.64	0.33
$\lambda_0/4$, Taylor-Padé	0.09	2.08e-5	1.4e-13
λ_0, Taylor-Padé	1.71	0.073	1.85e-10
$2.5\lambda_0$, Taylor-Padé	3.34	0.096	5.18e-5
$\lambda_0/4$, truncated products	2.38	1.04	0.35
λ_0, truncated products	7.35	3.19	1.06
$2.5\lambda_0$, truncated products	8.15	3.30	1.05

Fig. 15 The equivalent circuit of the numerical 1D model
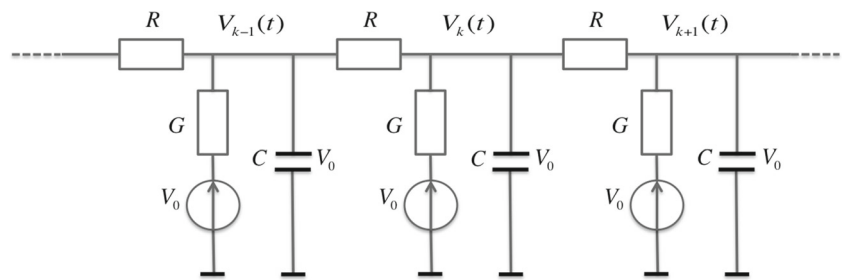
the infinite products takes into account both poles and zeros of original transfer functions. It balances both perspectives: current and voltage excitation. Figure 14 shows the way the relative error varies with the order of the reduced model, for different methods and $L = 2.5\lambda_0$.

Table 6 shows the relative errors of the reduced models (Y_{11} and Y_{12}, obtained by simple fractions, Taylor-Padé truncation and product truncation) for different line lengths and different orders (q), considering the analytical 1D model as reference.

With simple fractions reduction, Y_{12} has small relative errors, of less than 3% for large line and order 3. However, the deviations of Y_{11} for lengths of interest such as $2.5\lambda_0$ are much larger, of about 40% for order 1 and 20% for order 3. With Taylor-Padé reduction, both Y_{11} and Y_{12} have small relative errors, of 8% and 0.1% respectively, for large line and order 3. However, the deviation of Y_{11} for lengths of interest – such as $2.5\lambda_0$ – at order 1 is still quite large, of 31%. With product truncation reduction, Y_{11} has the smallest deviation at order 1, of less than 25%. For larger orders, the deviations of both Y_{11} and Y_{12} are similar and relatively small, but larger than the relative errors obtained with Taylor-Padé.

Therefore, the Taylor-Padé method gives the best approximation:

$$Y_{11}(s) = g\lambda_0 \frac{1 + \sum_{k=1}^{q} \frac{(L/\lambda_0)^{2k}(1+s\tau)^k}{(2k)!}}{L/\lambda_0 + \sum_{k=1}^{q} \frac{(L/\lambda_0)^{2k+1}(1+s\tau)^k}{(2k+1)!}};$$

$$Y_{12}(s) = g\lambda_0 \frac{1}{L/\lambda_0 + \sum_{k=1}^{q} \frac{(L/\lambda_0)^{2k+1}(1+s\tau)^k}{(2k+1)!}},$$

excepting Y_{11}, for order 4-7 where truncated products give better results.

For example, for $q = 4$ and $L = 2.5\lambda_0$, the four poles of the reduced model with truncated products are $p_1 = -3.85 \cdot 10^6$, $p_2 = -1.09 \cdot 10^7$, $p_3 = -2.27 \cdot 10^7$, $p_4 = -3.92 \cdot 10^7$ and the zeros are $z_1 = -2.08 \cdot 10^6$, $z_2 = -6.79 \cdot 10^6$, $z_3 = -1.62 \cdot 10^7$, $z_4 = -3.03 \cdot 10^7$, whereas G_{11} has a deviation of 0.35% from the d.c. value of admittance $Y_{11}(s)$.

3.3 Numerical 1D model: reduction by segmentation

Solving the Eq. (15) numerically implies the discretization of the interval $0 < x < L$ in a grid with q nodes (plus the

Fig. 16 Relative difference of potential from the exact value vs. the discretization step of the spatial network, in the stationary case
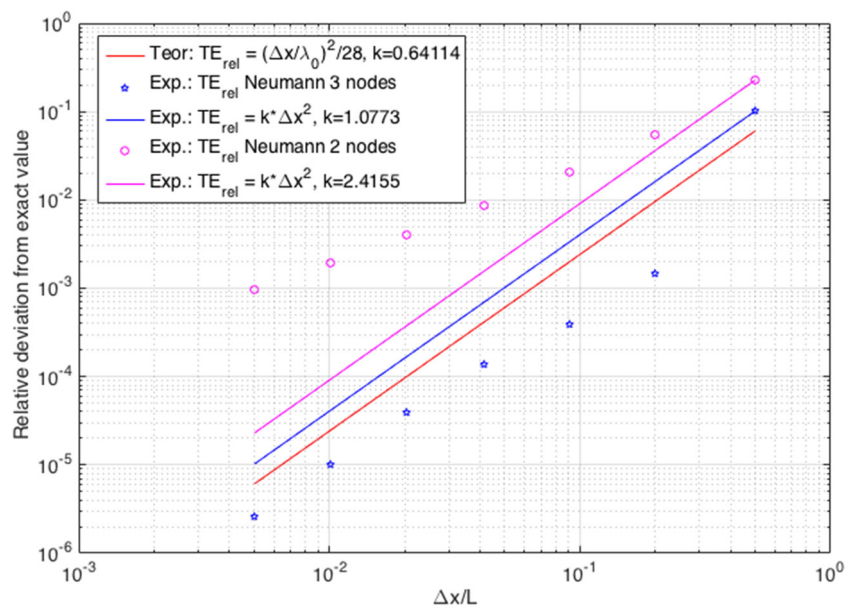
peripheral ones, indexed 0 and $q + 1$), which are assumed to be spaced with the step $h = \Delta x$. By finite centered differences, a system of q ODEs is obtained:

$$\frac{V_{k-1}(t) - 2V_k(t) + V_{k+1}(t)}{\Delta x^2} = \frac{1}{\lambda_0^2}(V_k(t) - V_0) + \frac{\tau}{\lambda_0^2}\frac{dV_k(t)}{dt}$$

$$k = 1, .., q; \; \frac{\Delta x^2}{\lambda_0^2} = rg\Delta x^2 = RG, \; \Delta x^2 \frac{\tau}{\lambda_0^2} = rc\Delta x^2 = RC,$$

$$\text{with } R = r\Delta x, \; G = g\Delta x, \; C = c\Delta x,$$

which after Laplace transform becomes:

$$-\frac{1}{R}V_{k-1}(t) + \left(\frac{2}{R} + G + sC\right)V_k(t) - \frac{1}{R}V_{k+1}(t) = GV_0.$$

These are actually the nodal equations of the circuit in Fig. 15, with $V_0 = 0$ and we will call this approach "reduction by segmentation". This circuit has q capacitors, so it is a linear circuit with q state variables.

Figure 16 shows the dependence of the relative error on the spatial step, theoretical (red) and experimental – calculated as the relative difference between the exact solution and the numerical solution in the stationary case. The numerical method has the order of convergence one if the Neumann condition at $x = L$ is discretized with regressive finite differences of order 1 (magenta), whereas if discretized with regressive finite differences of order 2 (blue), the method has the order of convergence two.

Having null internal sources ($V_0 = 0$) and controlling the terminals with $V_k = E = 1V$, for $k = 0$ and $V_{q+1} = 0$, the admittances are extracted by solving the linear system of nodal equations, from which only the first and the last potential are of interest: $Y_{11} = Y_{22} = (E - V_1)/R$ and $Y_{12} = Y_{21} = V_q/R$, numerically equal with the terminal currents. Table 7 shows the relative errors computed with Eq. (20) of the numerical models with 1, 3, 10, 100 segments for different orders (q), considering the analytical model (18) as reference, in the case of $L = 2.5\lambda_0$.

Table 8 shows the relative errors of the numerical model at f_m and f_M for different line lengths and different orders (q), considering the analytical 1D model as reference.

Table 7 The global relative errors of the numerical 1D model for $L = 2.5\lambda_0$, with respect to the analytical 1D model

$\varepsilon_{rel}[\%]$	$q = 1$	$q = 3$	$q = 10$	$q = 100$
Y_{11}	73.39	43.17	16.68	1.83
Y_{12}	24.83	2.75	0.25	1.96e-03

Table 8 The local relative errors of the numerical 1D model at f_m and f_M

L	$\varepsilon_{rel}[\%], q=3$		$\varepsilon_{rel}[\%], q=10$		$\varepsilon_{rel}[\%], q=100$	
	at f_m	at f_M	at f_m	at f_M	at f_m	at f_M
$\lambda_0/4$	25.1	24.7	9.13	8.63	0.99	0.93
λ_0	26.8	66.7	9.75	27.8	1.06	3.1
$2.5\lambda_0$	32.5	81.5	11.5	61.8	1.22	7.78

Second order finite centered differences have the order of error (De Sterck and Ullrich 2009):

$$|E_k| = |V_k - U_k| \leq \frac{(\lambda_0 h)^2}{12} = \frac{(L/\lambda_0)^2}{12q^2},$$

$$c_4 = \max_{0<x<L}\left(\left|\frac{\partial^4 V}{\partial x^4}\right|\right) \leq \frac{1}{\lambda_0^4},$$

quadratic to the discretization step. It is therefore expected that as q increases, the error decays inversely proportional to its square.

3.4 Order reduction of numerical 1D model

The numerical solving of the TL equation implicitly reduces the order, from infinite (the system order before meshing) to a finite number q. This technique of reducing the order is very widespread in the literature, and there are recommendations for choosing the value $5 \div 10$ for q (Moore et al. 1978). We are no aware of any credible study referring the error induced by this choice. However it is clear that the reduction by segmentation does not necessarily lead to an optimal result for a given order. We will find that smaller errors can be obtained for the same order if we reduce the state system of the circuit with n segments to a system with $q \ll n$ state variables. The equivalent circuit with refined segmentation has the state equations:

$$\frac{d}{dt}\begin{bmatrix} V_1 \\ .. \\ .. \\ .. \\ V_n \end{bmatrix} = \begin{bmatrix} .. & .. & .. & .. & .. \\ .. & -2 - RG & 1 & 0 & .. \\ .. & 1 & -2 - RG & 1 & .. \\ .. & 0 & 1 & -2 - RG & .. \\ .. & .. & .. & .. & .. \end{bmatrix}\begin{bmatrix} V_1 \\ .. \\ .. \\ V_q \end{bmatrix} + \begin{bmatrix} 1 \\ 0 \\ .. \\ .. \\ 0 \end{bmatrix}\frac{E}{R}$$

$$\Leftrightarrow \frac{d\mathbf{v}}{dt} = \mathbf{A}v + \mathbf{B}e; \; \mathbf{v} \in \mathbb{R}^{n\times 1}, \mathbf{A} \in \mathbb{R}^{n\times n}; \mathbf{B} \in \mathbb{R}^{n\times 1}.$$

The potentials V_1 and V_n are output signals, whereas E is the input signal of the system. This state system may be reduced by different model order reduction techniques, such as Heres (2005), Antoulas et al. (2001), and Panzer (2014):

– *Balanced truncation*

Balanced truncation (BT) has the most solid theoretical foundation. It is a projection method, based on the calculation of observability and controllability matrices of the system. Consequently, the cost of this method is relatively high, but the result is of optimal

quality, ensuring accuracy control for the reduced model (MATLAB 2015a).

The Bode diagrams of the 100-segments system and the characteristics of the reduced systems using balanced truncation to orders from 1 to 10 tend to close in as the q order rises. The poles and zeros of the reduced model of order 3 have the values: $z_1 = -405.54 \cdot 10^6$, $p_1 = -69.66 \cdot 10^6$; $z_2 = -10.13 \cdot 10^6$, $p_2 = -9.66 \cdot 10^6$; $p_3 = -2.21 \cdot 10^6$, real, negative and alternate, and $G_{11} = 0.812 \cdot 10^{-6}$ has a deviation of 4.91% from the d.c. value of admittance $\mathbf{Y}(s)$.

The model error drops below 1% only for orders $q > 6$, whereas for $q = 3$ it is about 10%, values about three times smaller than for the model obtained by simple segmentation.

– *Krylov Subspace (projection) methods*

In this class of methods, the state equations of large systems are reduced by projection on a Krylov subspace. They are considered to be among the best methods for order reduction from a quality – cost (computing effort) ratio point of view (Salimbahrami and Lohmann 2002; Berljafa and Güttel 2014).

The model reduced with this method from the state system with 100 degrees of freedom to $q = 2, 4, 6, 8, 10$ has the frequency characteristics practically overlayed with the full model, starting from $q = 4$. The errors are comparable with those obtained with the BT method, slightly smaller for $q = 4$ but larger for $q = 10$. In particular, the poles and zeros of the 4th order reduced system: $p_1 = -3055.81 \cdot 10^6$; $p_2 = -73.27 \cdot 10^6$; $p_3 = -12 \cdot 10^6$; $p_4 = -3.85 \cdot 10^6$; $z_1 = -5119.28 \cdot 10^6$; $z_2 = -357.91 \cdot 10^6$; $z_3 = -4.57 \cdot 10^6$ show the stable character of this model, and $G_{11} = 0.781 \cdot 10^{-6}$ is deviated by 0.85% from the d.c. value of admittance $\mathbf{Y}(s)$.

– *Proper Orthogonal Decomposition (POD)*

We used an in-house POD code based on Matlab's singular value decomposition method (MATLAB 2015b).

A standard neuronal signal was used as training excitation and the snapshots matrix contains solution values in $m = 100$ spatial nodes for $N = 100$ time samples.

The snapshots were generated with an in-house program based on BTCS integration (implicit backward finite difference in time, centered differences in space). The responses of the full system and the reduced one virtually overlap from order 3. For Y_{11}, the approximation is quite accurate, whereas for Y_{12}, the characteristic of the full system is concave, whereas for the reduced system is convex. The reduced system of order 3 has the poles: $p_1 = -38.12 \cdot 10^6$; $p_2 = -4.14 \cdot 10^6$; $p_3 = -1.49 \cdot 10^6$, with much smaller absolute

values than in previous cases, indicating that this model is slower. The conductance $G_{11} = 0.796 \cdot 10^{-6}$ has a deviation of 2.82% compared to the d.c. value of admittance $\mathbf{Y}(s)$. This method's error is higher than for the previous methods.

By comparing the results obtained with the three reduction methods, we conclude that the most efficient method for the studied case is the BT method.

4 Equivalent circuits for 0D models

The simplest model of an axon compartment is based on the lumped parameters:

$$R = L/(\sigma_1 \pi a^2); \tag{23}$$
$$C = L\varepsilon_2 2\pi/\ln(b/a); \tag{24}$$
$$G = L\sigma_2 2\pi/\ln(b/a), \tag{25}$$

extracted from uniform EC field in the cytoplasm and ES+EC fields in the axisymmetric membrane.

The equivalent circuit with these parameters has two possible symmetric topologies (Fig. 17): T-type and Π-type circuits, with the admittances matrices:

$$\mathbf{Y}_T = \begin{bmatrix} \frac{2R(G+sC)+4}{R^2(G+sC)+4R} & -\frac{4}{R^2(G+sC)+4R} \\ -\frac{4}{R^2(G+sC)+4R} & \frac{2R(G+sC)+4}{R^2(G+sC)+4R} \end{bmatrix};$$

$$\mathbf{Y}_\Pi = \begin{bmatrix} \frac{RG+sRC+2}{2R} & -\frac{1}{R} \\ -\frac{1}{R} & \frac{RG+sRC+2}{2R} \end{bmatrix}.$$

The advantages of these models lie in their simplicity and in the fact that they are inherently parametric. Within the accuracy of the calculation, these models are exact;
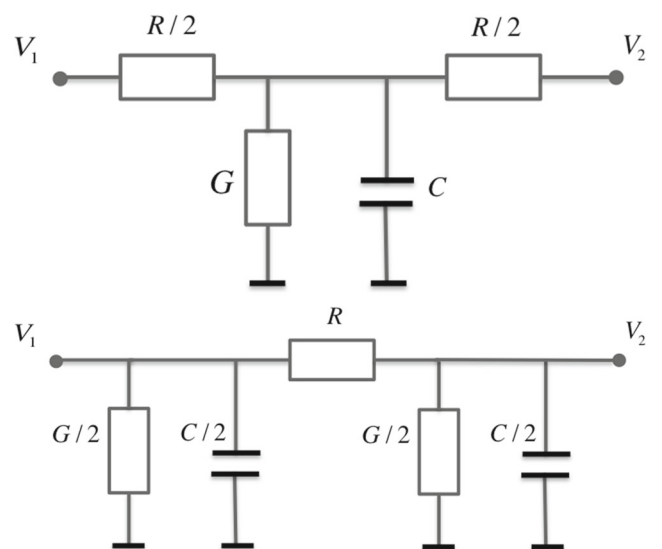

Fig. 17 The equivalent circuits of the 0D model; **a** T-type circuit; **b** Π-type circuit

Table 9 The admittance relative errors of 0D minimal order models

	$\varepsilon_T[\%]$ local		global		$\varepsilon_\Pi[\%]$ local		global	
L	at f_m	at f_M	Y_{11}	Y_{12}	at f_m	at f_M	Y_{11}	Y_{12}
$\lambda_0/4$	0.5	24.7	3.3	2.9	1.0	38.4	6.2	6.0
λ_0	7.5	81.1	19.8	6.1	15.5	271	33.5	19.2
$2.5\lambda_0$	32.1	91.5	48.7	1.2	73.9	748	114	24.8

therefore their analytical character make their numerical models alike. Even though the 0D model has large errors, it is frequently used in practice as reduced order model, due to its simplicity, even though its error is often not mentioned (Elmore 1948; Burger 2009). It is the model of order 1 with the smallest modeling error.

The relative errors of these two models, for 3 values of compartment lengths and 2 frequencies are given in Table 9, which contains also the global error for the two components Y_{11} and Y_{12}. The lumped parameter models with simpler Γ or $\Tau$ structures:

$$\mathbf{Y}_\Gamma = \begin{bmatrix} \frac{RG+sRC+1}{R} & -\frac{1}{R} \\ -\frac{1}{R} & \frac{1}{R} \end{bmatrix};$$

$$\mathbf{Y}_\Tau = \begin{bmatrix} \frac{1}{R} & -\frac{1}{R} \\ \frac{1}{R} & \frac{RG+sRC+1}{R} \end{bmatrix}.$$

have higher global errors for $L = 2.5\lambda_0$, of 298% for Y_{11} and 24.8% for Y_{12} (Γ) and of 73.3% for Y_{11} and 24.8% for Y_{12} ($\Tau$).

The data contained in Table 9 shows that this model has increasingly larger errors as the compartment length grows or as the frequency grows. The T-scheme behaves better for longer compartments, which are of practical interest ($2.5\lambda_0$ is the typical compartment length Bărbulescu et al. 2016), having a global error of 48.7% for Y_{11} and 1.2% for Y_{12}. If a better accuracy is required, higher order models, extracted by order reduction of 1D models should be used.

5 Simulation of full axons

In order to illustrate the use of linear models previously extracted for the modeling of myelinated axons with Ranvier nodes, we simulated the structure in Fig. 2b, consisting of one myelinated compartment and one Ranvier node. The model used for the linear myelinated part is the one which proved to give the best accuracy in our hierarchy: the 1D analytical model ($L = 2.5\lambda_0$) reduced


Fig. 18 The electric potential variation for the coupled model in three positions: **a** input of the linear compartment $e(t)$, **b** output of the linear compartment / input of the nonlinear block ($V_{lin}(t)$) **c** output of the nonlinear block $V_{nelin}(t)$
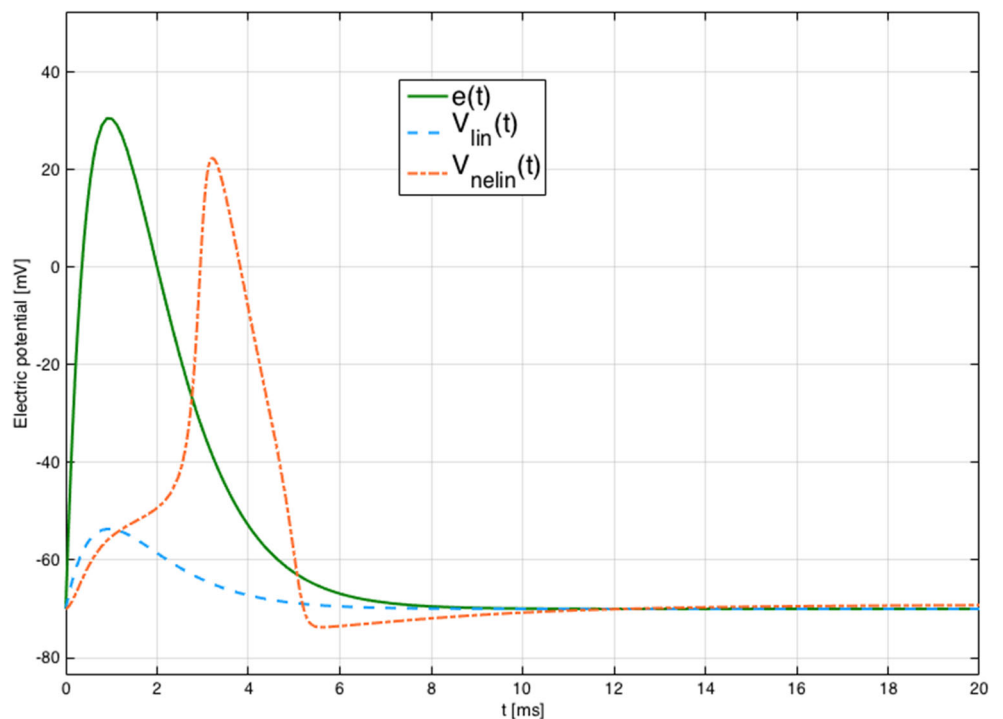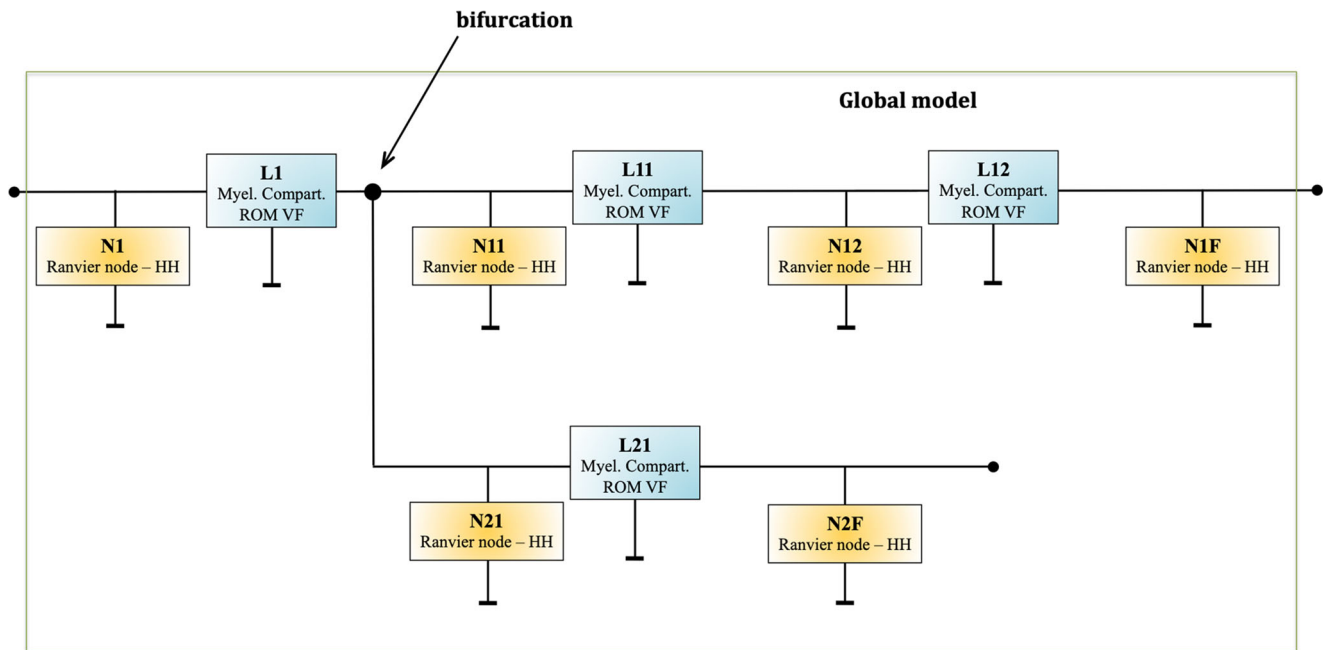
bifurcation

Fig. 19 The coupling of models in the global axon model is carried out in a circuit simulator. The blocks represent sub-circuits

Fig. 20 The electric potential at the output of every nonlinear node for: up) an axon with 3 sections Nx-Lx, no bifurcation; down) an axon with 2 branches, first with 3 sections Nx-Lx and second with one section Nx-Lx. The quantities are scaled: the time is in [ms], the potentials are in [mV] and the current in [nA]
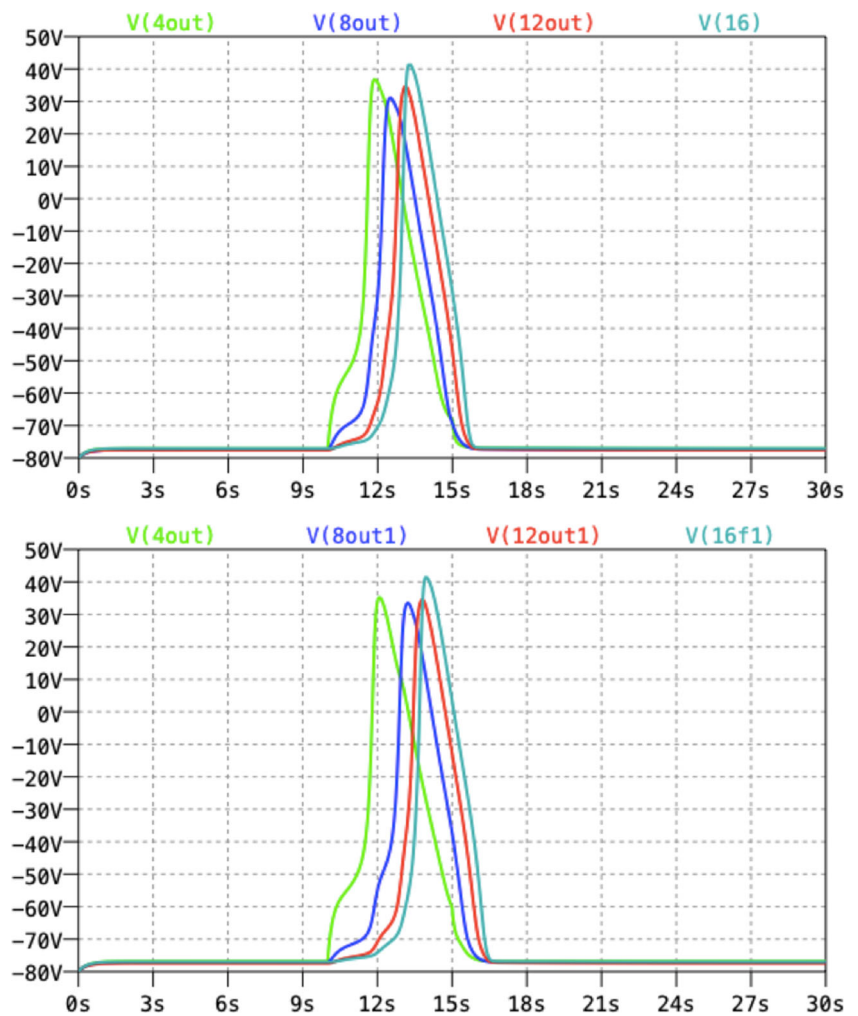
Table 10 The maximum amplitude and delay of the electric potential with and without bifurcation. The differences are emphasized by the bold figures

Signal node	Peak with bif. [mV]	Peak without bif. [mV]	$time_{peak}$ with bif. [ms]	$time_{peak}$ without bif. [ms]
N1 (4out/4out1)	35.17	36.75	12.098	11.9
N11 (8out/8out1)	**33.45**	**31.04**	**13.2**	**12.5**
N12 (12out/12out1)	34.5	34.6	**13.8**	**13.12**
N1F (16/16f1)	41.33	41.37	**13.94**	**13.26**

with VF, described by state space matrices. The Ranvier node was modeled as a nonlinear HH model (Hodgkin and Huxley 1952) with the parameters from Simulating action potential with the Hodgkin-Huxley model (2018), having $V_0 = -70$ mV as resting potential. The coupling was performed in Simulink / Matlab. The input signal is modeled as a difference of two exponentials, and the simulation time is 20 ms.

Figure 18 shows the variation of the electric potential for the coupled model at input, output of the linear compatment / input of the nonlinear model and at the output of the nonlinear model. In the absence of the Ranvier node the signal is strongly diminished as it diffuses along the myelinated compartment, whereas in the Ranvier node the signal is regenerated and delayed.

More structures of this kind Nx-Lx can be concatenated to form a longer myelinated axon, the chain being completed with a nonlinear bloc (Bărbulescu et al. 2019).

The global model obtained is nonlinear with reduced linear parts, therefore to simulate it one has to solve only ODEs instead of PDEs. This reproduces the phenomenon of saltatory conduction in myelinated axons for up to 500 sections (Bărbulescu et al. 2018).

The coupling is carried out in a circuit simulator as shown in Fig. 19. After the first section (N1-L1) we introduce a bifurcation and excite the left end of the axon with an impulse current of 20 nA, having a width of 5 ms. We compare the electric potential at the output of every nonlinear node of the first branch with and without bifurcation. Note in Fig. 20 that the maximum amplitude of the N11 signal (8out1) is lower in the presence of the bifurcation. Furthermore, all the signals of the nodes located after the bifurcation are more delayed than for a continuous chain with no bifurcation (signals 8out1, 12out1, 16f1; considering the time of their peak). Table 10 summarises these results.

Further discussion is required on the heterogeneous structures presenting different regions such as paranodal (MYSA) and juxtaparanodal (FLUT) regions at the beginning and end of the stereotyped, perfectly symmetrical internode region (STIN), as in Halter and Clark (1991). This heterogeneous model (Fig. 21) was simulated with FEM, and frequency characteristics very similar with the ones in Fig. 7 were obtained. Further, the model was reduced by vector fitting with a low error as in Fig. 22 (with relative errors under 1e-4, 1e-6 and 1e-8, for orders 3, 4 and 5 respectively). From the frequency characteristics we extracted a homogeneous structure by preserving the r and c line parameters and fitting g and the length by error minimization. The homogeneous model is ~9% longer and its conductance is ~20% higher than the STIN model. The new structure is able to approximate the heterogeneous admittances Y_{11} and Y_{12} with errors under 3% (2.71% for Y_{11} and 2.5% for Y_{12}). We therefore argue that these models can be approximated with enough accuracy with the behaviour of a homogeneous structure.
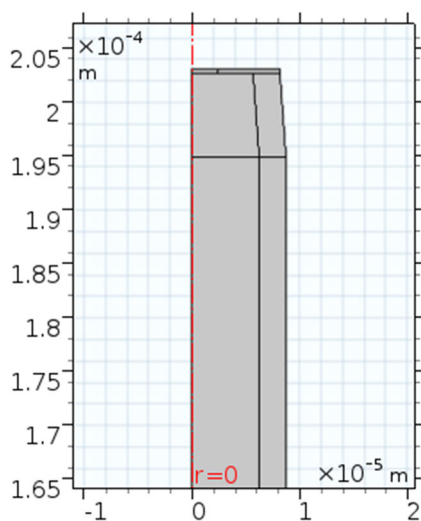
Fig. 21 The heterogeneous structure, section. Top: MYSA region; middle: FLUT region; bottom: part of STIN region

Table 11 Values of relative method errors for different models (analytical: the reference is extrapolated 2.5D FEM; numerical: the reference is the analytical model; reduced: the reference is the numerical model)

Size	Analytical	Numerical	Reduced
2.5D	0.026%	$7.5 \cdot 10^{-6}\%$	VF: 0.5% for $q = 3$; $3 \cdot 10^{-8}\%$ for $q = 9$
1D	0.057%	43% for $q = 3$; 16% for $q = 10$	Truncated products: 7% for $q = 3$; 0.8% for $q = 10$
			BT: 10% for $q = 3$; 0.1% for $q = 10$
0D	48.7% (for T-scheme)	48.7% (for T-scheme)	48.7% (for T-scheme)

6 Discussion and conclusions

In this study, the most accurate low-order models of myelinated compartments were identified. A hierarchical series of models has been developed, corresponding to three spatial geometry classes (2.5D, 1D and 0D) and three computational approaches for each geometry (analytical, numerical and reduced order models). These models are hierarchized based on modeling errors, which are closely related to the complexity of the models.

The errors computed with Eq. (20) for different types of models of the test problem are summarized in Table 11 (for $L = 2.5\lambda_0$). The simplest model is the circuit with lumped parameters (0D), but this model is not very accurate. The model with distributed parameters (cable model – 1D) is more accurate and was analyzed analytically by Laplace transformation from time domain to frequency and numerically with FDM for spatial variation. The order reduction was performed with several methods, such as: BT, projection on Krylov subspaces, POD and truncation of Taylor series or transfer function products. The most accurate model, the EQS axisymmetric (2.5D) was studied analytically using the method of variables separation (which leads to modal decomposition) and numerically with FEM, FIT and BEM methods – the most common methods used to solve PDEs. In this case, a data-driven approach (VF), was applied for order reduction. The numerical studies conducted show that the cable model (1D) is sufficiently accurate for practical requirements and it is not worth the effort to use 2.5D models in simulation.

Figure 22 shows how the relative method errors depend on the order of the reduced system, for different techniques of order reduction applied to various models.

The conclusion is that the most efficient reduction is done by the VF method, for which even for the first order the error is around 5%, and for orders 3 and 4 the error decays to 1% and to 0.1% respectively, which is satisfactory in the vast majority of practical cases. The next best method is the truncation (products and Taylor-Padé) of the transfer function (Fig. 22). The segmentation, which is currently the standard technique, provides results worse with at least two orders of magnitude.

In conclusion, there are two main contributions of this paper. First, it provides an answer to the questions: which

Fig. 22 Relative error vs. order of the reduced model
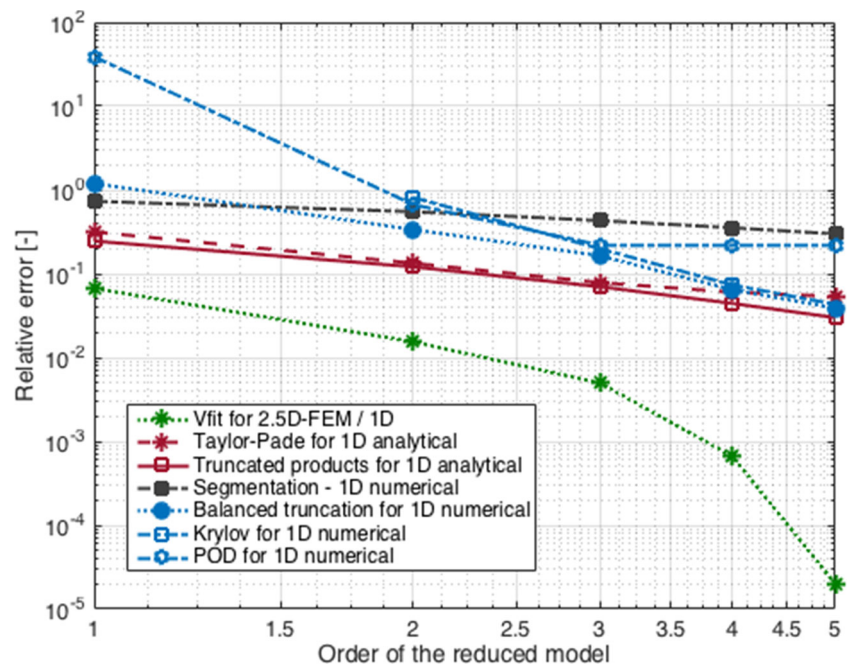
reduction method to an imposed order q has the best accuracy and what is the method able to reduce the model to the smallest order for an imposed error and what is the value of this order. Another contribution of the study consists in identifying how the model error should be defined, in order to provide a relevant characterization for the simulation of neuronal functioning. Our study proposes a weighted norm, suitably chosen for systems that transmit neural signals.

Finding the best low order model for myelinated compartments is an essential step in the modeling of neuronal signals transmission along myelinated axons through saltatory conduction. The 2.5D-FEM model is the most accurate, but the 1D cable model (in analytical form) is the most computationally efficient. Since the 1D and 2.5D responses are almost identical, for the modeling of the myelinated compartments we recommend the use of the analytical 1D model (18), followed by reduction to order $3 \div 4$, with vector fitting (VF). The time delay of the neural signal computed with the extracted model gives the speed of the signal transfer along the axon (Bărbulescu et al. 2016). This model allows to accurately determine not only the transmission speed of the neuronal signal, but also how this speed depends on geometrical and material parameters. Our source code is available upon request.

In the mathematical literature many methods of order reduction are presented and studied, but according to our knowledge, there is no systematic study referring to their hierarchy in neuroscience applications, leading to recommendations on which is the most appropriate method in a given context, such as the one studied here. Our study proves that the 1D cable model for axons that can be approximated with symmetrical geometries, or mild degrees of asymmetry and non-homogeneity can be as accurate as 3D models.

The methodology and tools developed throughout this study allow that a further increase of the morphological complexity which considers the periaxonal space (Gow and Devaux 2008) can be easily included, either by a small adaptation of the algorithm in the case of the analytical method or by a simple preprocessing step in the case of the numerical method. The impact that this extra current pathway could have is the subject of our ongoing research.

Compliance with Ethical Standards

Conflict of interests The authors declare that they have no conflict of interest.

Appendix : Derivation of the analytical (2.5D) model

The equation $\mathrm{div}(\sigma\,\mathrm{grad}\,V) = 0$, satisfied by the potential V in each homogeneous subdomain, has the following form in cylindrical coordinates:

$$\mathrm{div}\,(\sigma\,\mathrm{grad}\,V) = \frac{1}{r}\frac{\partial}{\partial r}\left(r\sigma\frac{\partial V}{\partial r}\right) + \frac{\partial}{\partial x}\left(\sigma\frac{\partial V}{\partial x}\right) = 0, \quad (26)$$

where the axial symmetry of the function (i.e. independence on the azimuthal angle) was taken into account. In each homogeneous subdomain the potential V is a harmonic function, a solution of the Laplace equation. According to the separation of variables method (Ioan 1988), in each homogeneous subdomain the potential V is assumed to have the form:

$$V(x, r) = X(x)R(r). \tag{27}$$

Substituting Eq. (27) in Eq. (26) it follows that the partial differential equation can be decomposed into two ordinary linear differential equations satisfied by the two functions X and R:

$$-\frac{1}{r}\frac{(\sigma r R')'}{\sigma R} = \frac{X''}{X} \Rightarrow \begin{cases} \frac{X''}{X} = \lambda^2 \\ -\frac{(\sigma r R')'}{\sigma r R} = \lambda^2, \end{cases} \tag{28}$$

where λ is a positive real constant, called constant of separation.

The solution of the first equation is:

$$X(x) = A\,\mathrm{sh}(\lambda x) + B\,\mathrm{ch}(\lambda x), \tag{29}$$

where A and B are integration constants.

In Eq. (28) σ is piecewise constant, (σ_1 for $0 < r < a$ and σ_2 for $a < r < b$). Therefore, on each homogeneous subdomain, the function R is the solution of the differential equation:

$$r^2 R'' + r R' + \lambda^2 r^2 R = 0,$$

which is a combination of zero order Bessel functions, with the following form for the general solution:

$$R(r) = C J_0(\lambda x) + D Y_0(\lambda x).$$

The parameter λ and the integration constants are derived by imposing the boundary conditions:

- on terminal 2 ($x = L$, $0 < r < a$):

$$\left.\frac{\mathrm{d}V}{\mathrm{d}n}\right|_{x=L} = 0 \Rightarrow X(x) = B'\mathrm{ch}(\lambda(L - x)),$$

$V(0, x)$ needs to have a finite value, so in the first subdomain ($0 < r < a$) D has to be zero and thus:

$$V(r, x) = C J_0(\lambda x)\mathrm{ch}(\lambda(L - x)). \tag{30}$$

After renaming the constants above, the potential has the general form:

$$V(r, x) = \begin{cases} B J_0(\lambda r)\mathrm{ch}(\lambda(L - x)), & 0 < r < a, \\ (C J_0(\lambda r) + D Y_0(\lambda r))\mathrm{ch}(\lambda(L - x)), & a < r < b. \end{cases}$$

- on the interface $r = a$:

$$V_1(a, x) = V_2(a, x), 0 < x < L$$

$$\left.\frac{\partial V_1}{\partial n}\right|_{r=a} = \beta \left.\frac{\partial V_2}{\partial n}\right|_{r=a}, \beta = \frac{\sigma_2 + j\omega\varepsilon_2}{\sigma_1 + j\omega\varepsilon_1} = \frac{\sigma_2}{\sigma_1}, \text{ for } \omega = 0.$$

It follows that:

$$\begin{cases} \frac{D}{C} = \left(\frac{1-\beta}{\beta}\right) / \left(\frac{Y_1(\lambda a)}{J_1(\lambda a)} - \frac{1}{\beta}\frac{Y_0(\lambda a)}{J_0(\lambda a)}\right); \\ \frac{B}{C} = 1 + \frac{D}{C}\frac{Y_0(\lambda a)}{J_0(\lambda a)} = 1 + \frac{(1-\beta)J_1(\lambda a)Y_0(\lambda a)}{\beta J_0(\lambda a)Y_1(\lambda a) - J_1(\lambda a)Y_0(\lambda a)}. \end{cases}$$

- on the boundary $r = b$:

$$V(b, x) = 0, \forall x \in [0, L] \Rightarrow C J_0(\lambda b) + D Y_0(\lambda b) = 0.$$

This leads to the eigenvalues equation:

$$(1 - \beta)Y_0(\lambda b)J_0(\lambda a)J_1(\lambda a) +$$
$$J_0(\lambda b)(\beta Y_1(\lambda a)J_0(\lambda a) - Y_0(\lambda a)J_1(\lambda a)) = 0,$$

which has an infinite number of solutions $\lambda_k, k = 1, 2, ..., \infty$ and the general solution of the problem $V(r, x)$ is obtained by superposition of all possible general forms:

$$V(r, x) = \begin{cases} \sum_k C_k \frac{B_k}{C_k} J_0(\lambda_k r)\mathrm{ch}(\lambda_k(L - x)), & 0 < r < a \\ \sum_k C_k (J_0(\lambda_k r) + \frac{D_k}{C_k}Y_0(\lambda_k r))\mathrm{ch}(\lambda_k(L - x)). \end{cases}$$

Equivalently:

$$V(r, x) = \sum_k C_k R(\lambda_{kr})\mathrm{ch}(\lambda_k(L - x)),$$

where R are eigenfunctions given by:

$$R(\lambda_{kr}) = \begin{cases} \frac{B_k}{C_k} J_0(\lambda_k r), & 0 < r < a \\ J_0(\lambda_k r) + \frac{D_k}{C_k}Y_0(\lambda_k r). & a < r < b \end{cases}$$

The constant C_k is computed by imposing the Neumann boundary condition at $x = 0$:

$$\left.\frac{\partial V}{\partial x}\right|_{x=0} = f(r),$$

$$f(r) = -\frac{I_1}{\sigma\pi a^2}h(a - r) = \begin{cases} -\frac{I_1}{\sigma\pi a^2}, & r \in (0, a) \\ 0, & r \in (a, b), \end{cases} \quad (31)$$

where h is the Heaviside function (unit step). The function $f(r)$ can be expanded into Fourier-Bessel series of eigenfunctions:

$$f(r) = \sum_{k=1}^{\infty} F_k R(\lambda_{kr}) = \sum_{k=1}^{\infty} C_k R(\lambda_{kr})\lambda_k \mathrm{sh}(\lambda_k L), \quad (32)$$

where the Fourier coefficients F_k of this series result from the orthogonality property of the eigenfunctions:

$$< R(\lambda_j r), R(\lambda_k r) > = \int_0^b r\sigma(r)R(\lambda_j r)R(\lambda_k r)\mathrm{d}r = 0, j \neq k.$$

In EC regime and with $j = k$ this relation becomes:

$$\|R_k\|^2 = \sigma_1 \int_0^a r\frac{B_k^2}{C_k^2}J_0^2(\lambda_k r)\mathrm{d}r +$$
$$\sigma_2 \int_a^b r(J_0(\lambda_k r) + \frac{D_k}{C_k}Y_0(\lambda_k r))^2\mathrm{d}r \Rightarrow$$

$$\|R_k\|^2 = \sigma_1 \frac{B_k^2}{C_k^2}\frac{a^2}{2}(J_0^2(\lambda_k a) + J_1^2(\lambda_k a))$$
$$+ \sigma_2\frac{1}{2}(b^2(J_0^2(\lambda_k b) + J_1^2(\lambda_k b))$$
$$- a^2(J_0^2(\lambda_k a) + J_1^2(\lambda_k a)))$$
$$+ \sigma_2\frac{D_k^2}{C_k^2}\frac{1}{2}(b^2(Y_0^2(\lambda_k b) + Y_1^2(\lambda_k b))$$
$$- a^2(Y_0^2(\lambda_k a) + Y_1^2(\lambda_k a)))$$
$$+ \sigma_2\frac{D_k}{C_k}(b^2(J_0(\lambda_k b)Y_0(\lambda_k b)$$
$$+ J_1(\lambda_k b)Y_1(\lambda_k b)) - a^2(J_0(\lambda_k a)Y_0(\lambda_k a)$$
$$+ J_1(\lambda_k a)Y_1(\lambda_k a))). \quad (33)$$

The scalar product between $R(\lambda_{kr})$ and $f(r)$ leads to the expression of F_k:

$$< R(\lambda_k r), f(r) > = F_k\|R_k\|^2 \Rightarrow$$
$$F_k = \frac{I_1}{\pi a^2\|R_k\|^2}\int_0^a rR(\lambda_{kr})\mathrm{d}r = \frac{I_1}{\pi a\|R_k\|^2}\frac{B_k}{C_k}\frac{1}{\lambda_k}J_1(\lambda_k a). \quad (34)$$

References

Abramowitz, M., Stegun, I.A., Romer, R.H. (1988). Handbook of mathematical functions with formulas, graphs and mathematical tables.

Antoulas, A.C., Sorensen, D.C., Gugercin, S. (2001). A survey of model reduction methods for large-scale systems. *Contemporary Mathematics*, *280*, 193–220.

Bărbulescu, R., Ioan, D., Ciuprina, G. (2018). Modeling the saltatory conduction in myelinated axons by order reduction. In *2018 20th international conference on neuroinformatics and computational neuroscience (ICNCN)* (pp. 2059–2062).

Bărbulescu, R., Ioan, D., Ciuprina, G. (2019). Coupled macromodels for the simulation of the saltatory conduction. Scientific Bulletin Series C (under review).

Bărbulescu, R., Ioan, D., Ciurea, J. (2016). Simple 1d models for neuro-signals transmission along axons. In *2016 international conference and exposition on electrical and power engineering (EPE)* (pp. 313–319): IEEE.

Berljafa, M., & Güttel, S. (2014). A rational Krylov toolbox for matlab.

Bower, J., & Beeman, D. (1998). The Book of GENESIS: exploring realistic neural models with the GEneral NEural SImulation System. Interpretation of Music; 55. TELOS. https://books.google.ro/books?id=WapQAAAAMAAJ. Accessed 14 Dec 2017.

Brain Facts and Figures (2017). https://faculty.washington.edu/chudler/facts.html#brain. Accessed 14 Dec 2017.

Brown, A.M., & Hamann, M. (2014). Computational modeling of the effects of auditory nerve dysmyelination. *Frontiers in Neuroanatomy 8*.

Burger, J.R. (2009). *Human memory modeled with standard analog and digital circuits: inspiration for man-made computers*. New Jersey: Wiley.

Carnevale, N.T., & Hines, M.L. (2006). *The NEURON book*. Cambridge: Cambridge University Press.

Ciuprina, G., Villena, J.F., Ioan, D., Ilievski, Z., Kula, S., ter Maten, E.J.W., Mohaghegh, K., Pulch, R., Schilders, W.H., Silveira, L.M., et al. (2015). Parameterized model order reduction. In *Coupled multiscale simulation and optimization in nanoelectronics* (pp. 267–359): Springer.

Clark, J., & Plonsey, R. (1966). A mathematical evaluation of the core conductor model. *Biophysical Journal*, *6*(1), 95–112.

De Sterck, H., & Ullrich, P. (2009). Introduction to computational pdes. Course Notes for Amath 442.

Digicortex (2017). http://www.digicortex.net/. Accessed: 2017-12-14.

Elmore, W.C. (1948). The transient response of damped linear networks with particular regard to wideband amplifiers. *Journal of Applied Physics*, *19*(1), 55–63.

Fitzhugh, R. (1962). Computation of impulse initiation and saltatory conduction in a myelinated nerve fiber. *Biophysical Journal*, *2*(1), 11–21.

FitzHugh, R. (1966). Mathematical models of excitation and propagation in nerve. Publisher Unknown.

Frankenhaeuser, B., & Huxley, A. (1964). The action potential in the myelinated nerve fibre of xenopus laevis as computed on the basis of voltage clamp data. *The Journal of Physiology*, *171*(2), 302–315.

Ganapathy, N., & Clark, J. (1987). Extracellular currents and potentials of the active myelinated nerve fiber. *Biophysical Journal*, *52*(5), 749–761.

Goldman, L., & Albus, J.S. (1968). Computation of impulse conduction in myelinated fibers; theoretical basis of the velocity-diameter relation. *Biophysical Journal*, *8*(5), 596–607.

Gow, A., & Devaux, J. (2008). A model of tight junction function in central nervous system myelinated axons. *Neuron Glia Biology*, *4*(4), 307–317.

Graham, B., Gillies, A., Willshaw, D. (2011). Principles of computational modelling in neuroscience.

Graupner, M., & Brunel, N. (2010). Mechanisms of induction and maintenance of spike-timing dependent plasticity in biophysical synapse models. *Frontiers in Computational Neuroscience 4*.

Gurney, K. (1997). *An introduction to neural networks*. Boca Raton: CRC Press.

Gustavsen, B., & Semlyen, A. (1999). Rational approximation of frequency domain responses by vector fitting. *IEEE Transactions on Power Delivery*, *14*(3), 1052–1061.

Halter, J.A., & Clark, J.W.Jr.. (1991). A distributed-parameter model of the myelinated nerve fiber. *Journal of Theoretical Biology*, *148*(3), 345–382.

Haykin, S. (1999). Neural networks: a comprehensive foundation. International edition. Prentice Hall. https://books.google.ro/books?id=M5abQgAACAAJ.

Heres, P.P. (2005). Robust and efficient Krylov subspace methods for model order reduction. Ph.D. thesis, Technische Universiteit Eindhoven.

Hodgkin, A.L., & Huxley, A.F. (1952). A quantitative description of membrane current and its application to conduction and excitation in nerve. *The Journal of Physiology*, *117*(4), 500–544.

Huxley, A., & Stämpeli, R. (1949). Evidence for saltatory conduction in peripheral myelinated nerve fibres. *The Journal of Physiology*, *108*(3), 315–339.

Ioan, D. (1988). Metode pentru calculul campului electromagnetic. Separarea variabilelor. IPB.

Ioan, D., Ciuprina, G., Radulescu, M., Seebacher, E. (2006). Compact modeling and fast simulation of on-chip interconnect lines. *IEEE Transactions on Magnetics*, *42*(4), 547–550.

Ioan, D., & Munteanu, I. (1999). Missing link rediscovered: the electromagnetic circuit element concept. *JSAEM Studies in Applied Electromagnetics and Mechanics*, *8*, 302–320.

Izhikevich, E.M. (2003). Simple model of spiking neurons. *IEEE Transactions on Neural Networks*, *14*(6), 1569–1572.

Izhikevich, E.M. (2007). *Dynamical systems in neuroscience*. Cambridge: MIT Press.

Jin, J.M. (2015). *The finite element method in electromagnetics*. New Jersey: Wiley.

Joucla, S., Glière, A., Yvert, B. (2014). Current approaches to model extracellular electrical neural microstimulation. *Frontiers in Computational Neuroscience 8*.

Keener, J., & Sneyd, J. (2010). Mathematical physiology: I: cellular physiology. Springer Science & Business Media.

Kuokkanen, P. (2012). On the origin of the extracellular potential in the nucleus laminaris of the barn owl. Ph.D. thesis, Humboldt-Universität zu Berlin, Mathematisch-Naturwissenschaftliche Fakultät I.

Lindsay, K., Ogden, J., Halliday, D., Rosenberg, J. (1999). An introduction to the principles of neuronal modelling. In *Modern techniques in neuroscience research* (pp. 213–306): Springer.

Lozier, D.W. (2003). Nist digital library of mathematical functions. *Annals of Mathematics and Artificial Intelligence*, *38*(1), 105–119.

Maass, W. (1997). Networks of spiking neurons: the third generation of neural network models. *Neural Networks*, *10*(9), 1659–1671.

MATLAB (2015). Balanced model truncation via square root method. The MathWorks Inc., Natick, Massachusetts.

MATLAB (2015). Singular value decomposition. The MathWorks Inc., Natick, Massachusetts.

Moore, J., Ramon, F., Joyner, R. (1975). Axon voltage-clamp simulations. i. methods and tests. *Biophysical Journal*, *15*(1), 11–24.

Moore, J.W., Joyner, R.W., Brill, M.H., Waxman, S.D., Najar-Joa, M. (1978). Simulations of conduction in uniform myelinated fibers. relative sensitivity to changes in nodal and internodal parameters. *Biophysical Journal*, *21*(2), 147–160.

Morrison, A., Diesmann, M., Gerstner, W. (2008). Phenomenological models of synaptic plasticity based on spike timing. *Biological Cybernetics*, *98*(6), 459–478.

Niebur, E. (2008). Neuronal cable theory. *Scholarpedia*, *3*(5), 2674.

Panzer, H. (2014). Model order reduction by Krylov subspace methods with global error bounds and automatic choice of parameters. Verlag Dr. Hut.

Parasuram, H., Nair, B., D'Angelo, E., Hines, M., Naldi, G., Diwakar, S. (2016). Computational modeling of single neuron extracellular electric potentials and network local field potentials using lfpsim. Frontiers in Computational Neuroscience 10.

Paugam-Moisy, H., & Bohte, S. (2012). Computing with spiking neuron networks. In *Handbook of natural computing* (pp. 335–376): Springer.

Rapetti, F., & Rousseaux, G. (2014). On quasi-static models hidden in Maxwell's equations. *Applied Numerical Mathematics*, *79*, 92–106.

Rattay, F., Potrusil, T., Wenger, C., Wise, A.K., Glueckert, R., Schrott-Fischer, A. (2013). Impact of morphometry, myelinization and synaptic current strength on spike conduction in human and cat spiral ganglion neurons. *PLoS One*, *8*(11), e79,256.

Robinson, P., Rennie, C., Rowe, D., O'Connor, S., Gordon, E. (2005). Multiscale brain modelling. *Philosophical Transactions of the Royal Society of London B: Biological Sciences*, *360*(1457), 1043–1050.

Salimbahrami, B., & Lohmann, B. (2002). Krylov subspace methods in linear model order reduction: introduction and invariance properties. In *Sci. Rep. Inst. of Automation. Citeseer*.

Simulating action potential with the Hodgkin-Huxley model (2018). https://www.comsol.com/model/simulating-action-potential-with-the-hodgkin-huxley-model-47121. Accessed: 2018-06-10.

Stephanova, D. (2001). Myelin as longitudinal conductor: a multi-layered model of the myelinated human motor nerve fibre. *Biological Cybernetics*, *84*(4), 301–308.

Stoica, P., Moses, R.L., et al. (2005). *Spectral analysis of signals* Vol. 452. Upper Saddle River: Pearson Prentice Hall.

Struijk, J.J., Holsheimer, J., van der Heide, G.G., Boom, H.B. (1992). Recruitment of dorsal column fibers in spinal cord stimulation: influence of collateral branching. *IEEE Transactions on Biomedical Engineering*, *39*(9), 903–912.

Timotin, A. (2004). La structure de la fibre nerveuse: Un projet optimal. Proceedings of the Romanian Academy Series A 5(1).

The Nervous System (2017). (Structure and function) (Nursing) part 1. http://what-when-how.com/nursing/the-nervous-system-structure-and-function-nursing-part-1/ . Accessed: 2017-12-14.

Van Geit, W., De Schutter, E., Achard, P. (2008). Automated neuron model optimization techniques: a review. *Biological Cybernetics*, *99*(4-5), 241–251.

Villapecellín-Cid, M.M., Medina, F., Roa, L.M. (2004). Internodal myelinated segments: delay and rgc time-domain green function model. *IEEE Transactions on Biomedical Engineering*, *51*(2), 389–391.

Young, R. (2015). Mathematical modeling of the evolution and development of myelin. Ph.D. thesis, University of Hawaii at Manoa.